JOURNAL OF GEOPHYSICAL RESEARCH, VOL. 113, C07031, doi:10.1029/2007JC004677, 2008

Click Here for Full Article

Baroclinic tides in the Indonesian seas: Tidal fields and comparisons to observations

Robin Robertson[1] and Amy Ffield[2]

Received 6 December 2007; revised 11 February 2008; accepted 22 April 2008; published 22 July 2008.

[1] Barotropic and baroclinic tides were simulated for the Indonesia Seas using a primitive equation, terrain-following coordinate model, the Regional Ocean Model System (ROMS) with four tidal constituents (M_2, S_2, K_1, and O_1). The region's intricate topography as well as interactions between the Pacific and Indian Ocean tides within the Indonesian Seas resulted in complex barotropic and baroclinic tidal fields. The semidiurnal tides entered from both the Pacific and Indian oceans converging in Makassar Strait and the Ceram Sea with an amphidromic point forming in the Timor Sea. Diurnal tides were dominated by the Pacific Ocean tide. The model successfully replicated the observed tidal elevation fields as determined from TOPEX/POSEIDON crossovers with better performance for the semidiurnal constituents, RMS differences of 4–6 cm, than the diurnal constituents, RMS differences of 7–10 cm. A baroclinic response was apparent in the elevations, and the locations of the observed baroclinic elevation response in TOPEX/POSEIDON data agreed with that of the model. Velocities were baroclinic for all constituents with high spatial variability, particularly near sills and in straits. Extensive interactions occurred in the internal tidal fields: between a beam and its own reflections, between internal tides generated at different locations (i.e., different sides of a channel, or beams generated nearby), and between the barotropic and baroclinic tidal beams. Owing to propagation, even regions >100 km from sills showed significant vertical and horizontal variability resulting from internal tides. This resulted in extremely complex internal tidal fields with high variability, both spatially and temporally during a tidal cycle.

Citation: Robertson, R., and A. Ffield (2008), Baroclinic tides in the Indonesian seas: Tidal fields and comparisons to observations, *J. Geophys. Res.*, *113*, C07031, doi:10.1029/2007JC004677.

1. Introduction

[2] In the Indonesian Seas (Figure 1a), North and South Pacific Waters enter from the north with a distinctive subsurface salinity signature and exit in the south into the Indian Ocean as Indonesian Throughflow Water having lost the salinity signature [*Gordon*, 2005]. Along the way, the water masses are transformed by the Indonesian "mix-master" converting the high salinities associated with the North and South Pacific waters and the low salinities associated with the North Pacific Intermediate water into a water mass with a nearly uniform salinity below 100 m [*Ffield and Gordon*, 1992; *Hautala et al.*, 1996; *Gordon*, 2005]. This water mass transformation is accomplished through mixing, with the primary mixing mechanism believed to be tidal [*Hatayama et al.*, 1996; *Hatayama*, 2004; *Gordon*, 2005]. Observations support this view of tides as the primary vertical mixing mechanism in the Indonesian Seas [*Ffield and Gordon*, 1992, 1996].

[3] To understand the tidal mixing, its extent, and where it occurs, and to estimate its mixing contribution, the tidal fields must be known. Much of the mixing occurs owing to the internal or baroclinic tide [*Munk and Wunsch*, 1998; *Garrett*, 2003], which results from interactions between topographic features and the barotropic tide. Thus, not only do the tidal elevations need to be known, but also the barotropic and baroclinic velocity fields.

[4] Barotropic tides have been simulated for the Indonesian Seas by *Hatayama et al.* [1996], *Mazzega and Bergé* [1994], *Egbert and Erofeeva* [2002], and *Ray et al.* [2005] with good results in replicating observed barotropic tidal elevations and currents for various numbers of constituents. *Hatayama et al.* [1996] estimated the effects of the barotropic tides for two constituents on transport and mixing, but did not include baroclinic tidal contributions. Their results indicated intense vertical mixing in the southwestern portion of the Makassar Strait and other shallow regions from the barotropic tide.

[5] However, none of these simulations addressed the baroclinic tides. Baroclinic tides were simulated for this region by *Schiller* [2004] and *Robertson and Ffield* [2005]. In order to more fully resolve the internal tidal signals, simulations of baroclinic tides require a resolution of 5 km

[1]Australian Defence Force Academy, University of New South Wales, Canberra, ACT, Australia.
[2]Earth and Space Research, Upper Grandview, New York, USA.

Copyright 2008 by the American Geophysical Union.
0148-0227/08/2007JC004677$09.00

or higher [*Robertson*, 2006]. *Schiller*'s [2004] simulation was global with a resolution of 0.5° (~52–57 km) in longitude and 0.33° (~37 km) in latitude, which was appropriate for the global scope. *Robertson and Ffield* [2005] simulated the baroclinic tides at a resolution of 5 km, but only for one tidal constituent, M_2. Although this was a good start, it neglected interactions between constituents.

[6] In this study, both the barotropic and baroclinic tides were simulated at a resolution of 5 km for the Indonesian Seas (Figure 1) with forcing by the four major tidal constituents (M_2, S_2, K_1, and O_1). The simulations were compared to observations to evaluate model performance. The model used for the simulations will be described in section 2. Observations used for the comparison are outlined in section 3 with the results of the comparisons given for tidal elevations in section 4, tidal velocities in Section 5, and composite fields in section 6. A summary is given in section 7. Implications of the model results and interactions between constituents with a focus on Ombai Strait are discussed in a companion paper (R. Robertson and A. Ffield, Baroclinic tides in the Indonesian Seas: 2. Interactions between tidal constituents, energy fluxes, and tidal mixing with a focus on Ombai Strait, submitted to *Journal of Geophysical Research*, 2008).

2. Model Description

2.1. Model

[7] Version 1.7.3 of the Regional Ocean Model System (ROMS), a terrain-following, primitive-equation model developed by the Ocean Modeling group at Rutgers University, was used (http://www.ocean-modeling.org/index.php?page=models&model=ROMS) for the simulations. Terrain following models, such as ROMS and the widely used Princeton Ocean Model (POM), have the advantage that the grid cells adjust in height according to the topography, allowing the model to be used for domains with widely varying water depths. This is key for the Indonesian Seas, where water depths vary from less than 50 m in the Java and Arafura Seas to over 7000 m in the deep trenches of the Banda Sea. Since ROMS is hydrostatic, internal solutions will not be simulated in the model.

[8] One reason ROMS was selected was its wide array of available options for different numerical schemes and parameterizations that can be tailored for regional studies. ROMS uses split 2-D (barotropic) and 3-D (baroclinic) modes to obtain the required temporal resolution for the 2-D mode without the high calculation overhead necessary for the 3-D model. For these simulations, third-order upstream differencing was used for horizontal advection, *Laplacian* lateral diffusion was determined along geopotential surfaces (10 m^2 s^{-1}) [*Shchepetkin and McWilliams*, 2003], and the splines density Jacobian scheme was used for the baroclinic pressure gradient calculation. Vertical mixing was determined according to the Generic Length Scale (GLS) parameterization of *Umlauf and Burchard* [2003] and *Umlauf et al.* [2003] using their generic option (with $m = 1$, $n = -0.67$, and $p = 1$) [*Warner et al.*, 2005]. These options were selected on the basis of the results of a sensitivity study on model operating parameters for a baroclinic tidal simulation of the region around Fieberling Guyot [*Robertson*, 2006]. ROMS has been utilized for barotropic and baroclinic tidal modeling by investigators [*Robertson et al.*, 2003; *Robertson*, 2005a, 2005b; *Robertson and Ffield*, 2005; R. Hetland, personal communication, 2001].

2.2. Domain

[9] *Smith and Sandwell* [1997] bathymetry was used for the topography over the domain (dashed (yellow) box in Figure 1a), which covered much of the Indonesian Seas. At a 5 km resolution, this resulted in a grid of 448 cells by 480 cells. The 0 m isobath was used as the coastline and water depths shallower than 50 m were deepened to 50 m for modeling stability considerations and to keep time steps size reasonable. Shallow regions are generally well mixed and unlikely locations of internal waves, so deepening these regions has little impact on the focus of the research. In areas where the topographic steepness as characterized by r-factors exceeded 0.4, bathymetry was smoothed using multiple passes of a Gaussian weighted window with a width of 3 cells in each direction. This reduced the number of points with r-factors exceeding 0.4 from 16,408 values, with a maximum of 0.95, to 8500. Further passes of the filter did not change the number of points exceeding 0.4 and most of these points were located in shallow water. A resolution of 5 km was used in the horizontal directions and 24 levels were used in the vertical direction with closer spacing in both the surface and benthic boundary layers (Figure 1b).

2.3. Initial Conditions

[10] Initial hydrography, consisting of potential temperature, θ, and salinity, S, fields, was obtained from the National Oceanographic Data Center (http://www.nodc.noaa.gov/General/getdata.html) and interpolated onto the domain. The model was run for 30 days without tidal forcing to allow geostrophic and density driven velocities to develop and stabilize. These velocities were used as initial conditions for subsequent simulations.

2.4. Boundary Conditions and Forcing

[11] Boundary conditions were set for elevation, velocities, temperature, and salinity. With velocity, different boundary conditions were used for the barotropic and baroclinic modes. The barotropic mode velocities used Flather radiative boundary conditions in the normal direction [*Flather and Proctor*, 1983] and advective conditions in the tangential directions. The baroclinic velocities used flow relaxation boundary conditions to initial conditions over four cells as described by *Martinsen and Engedahl* [1987]. Similarly for the temperature and salinity, the boundary values were relaxed over four cells. There were no fluxes through the surface or bottom for temperature or salinity and the volume was unconstrained. No incoming solar radiation or precipitation was prescribed and there were no surface fluxes. Mean currents were also not prescribed along open boundaries.

[12] Tidal forcing was implemented through the elevations along the boundary updated at every 2-D time step, with complex coefficients taken from a 2-D model, *Egbert and Erofeeva*'s [2002] global inverse tidal model (OTIS). Velocity boundary conditions were not used, although that is a commonly done with ROMS. Four major tidal constituents were simulated, two semidiurnals, M_2 and S_2, and

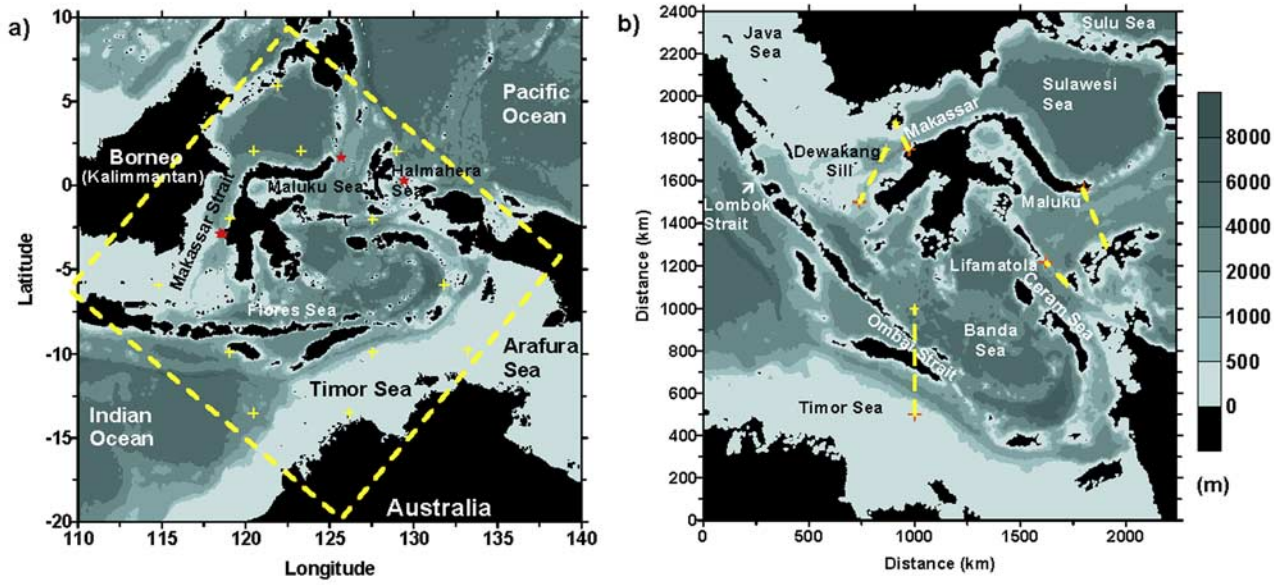

Figure 1. (a) The bathymetry of the Indonesian Seas with identification of some of the major features. The model domain is indicated by a dashed box, and the locations of TOPEX/POSEIDON crossover elevation observations are indicated by crosses. Current meter mooring locations in the Makassar Strait and Maluku and Halmahera Seas are marked with stars. (b) The bathymetry over the model domain. Transect locations of Figure 9 are indicated by dashed lines with a cross at the origin.

two diurnals, K_1 and O_1. Tidal elevations were updated every 2-D time step.

2.5. Operational Considerations

[13] The 2-D (barotropic) and 3-D (baroclinic) mode time steps for the base case were 2 s and 60 s, respectively, and all simulations were run for 20 days, with hourly data from the last 15 days used for analysis. Kinetic and potential energies stabilized around 5 days, thus the first 5 days of simulated data were discarded.

2.6. Model Outputs

[14] The model produced fields for the elevation, η, and depth-independent horizontal velocities, U_2 and V_2, from the 2-D (barotropic) mode of the model. Potential temperature, θ, salinity, S, and depth-dependent velocities, U_3, V_3, and W_3, fields were generated by the 3-D (baroclinic) mode. The depth-dependent velocities comprise the complete velocity from the equations of motion, and are not perturbations from the 2-D velocities. *Foreman*'s [1977, 1978] tidal analysis routines were used to analyze the elevation and velocity fields, respectively, and generate the tidal ellipse parameters for the four constituents, M_2, S_2, K_1, and O_1.

3. Observational Data

[15] Since these simulations were intended to be realistic scenarios, comparisons against observational data were used to evaluate the model performance. Two types of data were involved: satellite-derived sea surface elevation data and in situ velocity data.

3.1. Tidal Elevations

[16] TOPEX/POSEIDON (T/P) satellite altimeter was used to evaluate the barotropic and the combined barotropic and baroclinic contributions to the tidal elevations. The length of the series at the locations varied since T/P orbits shifted in 2001, but typically 9–13 years of data spaced at 9.92 days were used for analysis. Locations with time series less than 2.5 years in length were ignored. The barotropic contributions are based on T/P crossover data, which has coherent length scales on the order of thousands of kilometers. Thirteen crossover points (plus signs in Figure 1a and crosses in Figure 2) fell within the domain and were used to estimate the barotropic tidal amplitudes and phases for the four constituents (Table 1).

[17] A technique for estimating tidal elevations including the baroclinic contribution by the tidal constituents was developed by *Ray and Mitchum* [1997]. In this technique, time series are constructed for points along the T/P ascending and descending tracks and analyzed for the tidal constituents using least squares analysis. Along-track data for the Indonesian Seas were obtained from NASA via netftp/pub/sea_surface_height./TOPEX_poseidon/mgdrb and analyzed following *Ray and Mitchum*'s [1997] procedure with information from R. W. Berwin (Along-track gridded sea surface height anomaly for TOPEX/POSEIDON and Jason-1 User's Reference Manual Version 2, 2003, ftp://podaac.jpl.nasa.gov/pub/sea_surface_height/topex_poseidon/tp_atg/doc/along_track_gridded_manual_v2.html, NASA/JPL). A 150 km low-pass filter was used to separate the barotropic and baroclinic tidal responses. Tidal estimates for the combined barotropic and baroclinic tidal elevation amplitude and phase for different constituents were calculated along the tracks at a spacing of ~5.5 km (thin black lines in Figures 3a–3d). This technique was applied to the ascending and descending T/P tracks to obtain estimates of the M_2 amplitude and phase (thin black lines in Figures 3a–3d and 4) including the baroclinic contributions. Both ascending and

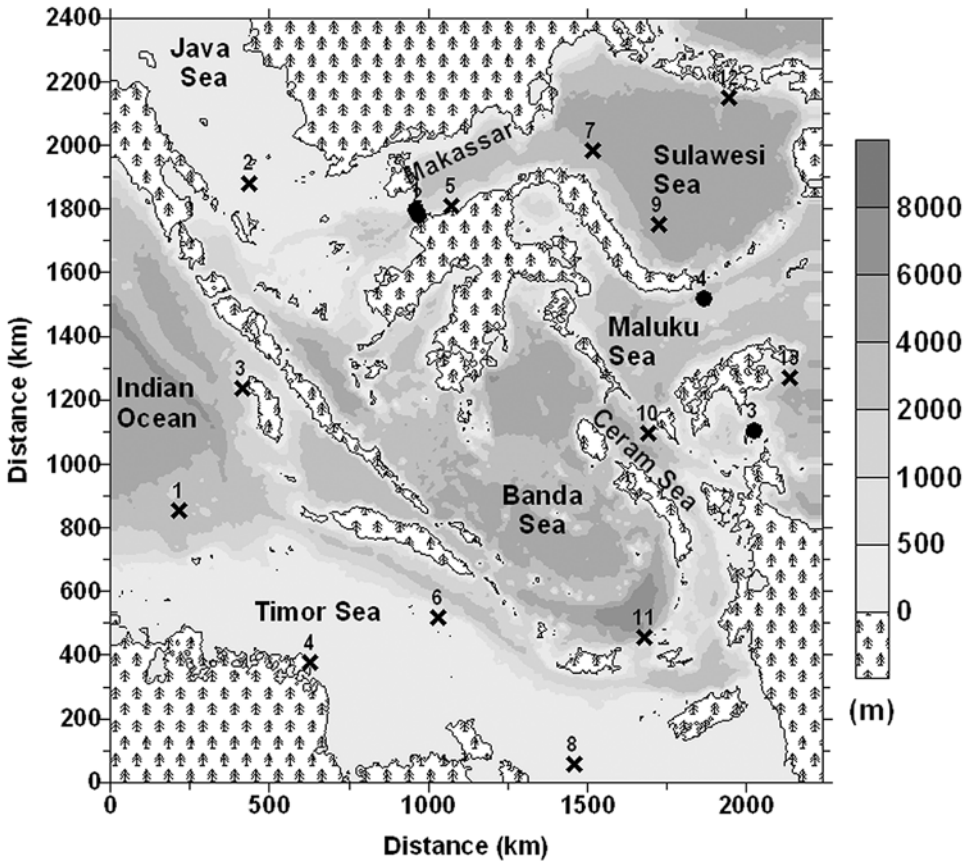

Figure 2. Locations of TOPEX/POSEIDON crossover observations within the model domain are indicated by crosses and numbered corresponding to Table 1.

descending tracks can be seen in Figure 4, with the ascending tracks increasing in latitude from left to right and the descending tracks decreasing in latitude from left to right.

[18] Barotropic and baroclinic tidal contributions can be easily separated, since their length scales and propagation are quite different. Barotropic tides propagate basin-wide, whereas baroclinic tides are local phenomena. Barotropic tidal length scales are large, thousands or kilometers, compared to baroclinic length scales, with a maximum of ~250 km and more typical semidiurnal values ranging from 50 to 100 km. In order to separate barotropic and baroclinic portions, a 150 km wide filter with weighting dependent on the square root of the distance was applied. The barotropic tidal amplitudes (thick gray lines in Figures 3a and 3f) are smoother versions of the combined tide (thin black lines in Figures 3a and 3f). And the barotropic amplitudes (thick gray line in Figures 3a and 3f) are much smoother and larger than the baroclinic amplitudes (Figures 3c and 3g), which fell within ±10 cm. In general, features in the combined baroclinic and barotropic amplitude, which deviated from the barotropic amplitude and have length scales of ~50–150 km could potentially be baroclinic tidal signals, although they may not necessarily be baroclinic tides (Figures 3a and 3f).

[19] There are some concerns with the along-track tidal estimates. Estimates from the ascending and descending tracks were determined independently and did not always agree. Phases were relatively consistent both between the ascending and descending tracks (lines in Figure 4b) and with the estimates from the crossovers (plus signs in Figure 4b), although there are some deviations such as between 2° and 0° S along ascending track 7 (Figure 3b). Amplitudes between the ascending and descending tracks were not always consistent, with disagreement in several locations (Figure 4a). For example, in the region between Australia and Indonesia, amplitudes of 80–90 cm were predicted from the ascending track and of 70–80 cm from the descending track. The crossover at that location (site 1) had a value of 83.1 cm for M_2 (Table 1) supporting the ascending track estimate. Also in some locations, the crossover estimates differed from the estimates of the ascending and descending tracks with a tendency of the along-track estimates to be smaller than the crossovers. This was particularly noticeable in the Sulawesi Sea where the crossover locations (sites 7, 9, and 12) have values from 57 to 60 cm (plus signs in Figure 4a) and the ascending and descending tracks estimates are 20–40 cm (Figure 4a), roughly a factor of two smaller. In these cases of disagreement, the crossover values were believed to be more accurate.

[20] There are other concerns with the along-track estimates. First, they are influenced by factors other than baroclinic tides, basically anything that affects surface elevation such as bathymetry, eddies, shallow water effects, atmospheric pressure, etc. Tidal analysis should eliminate these factors unless they alias into the tidal frequency, but potential for contamination remains.

Table 1. Elevation Amplitude and Phases at the 13 T/P Crossover Locations From the T/P Crossover Data and the ROMS Simulation[a]

Site Latitude Longitude	Observation/Model/ Difference	M_2		S_2		K_1		O_1	
		Amp. (cm)	Phase (o)	Amp. (cm)	Phase (o)	Amp. (cm)	Phase (o)	Amp. (cm)	Phase (o)
1	T/P Crossover	89.7	56	50.0	130	24.1	169	14.1	161
13°31′S	ROMS	95.2	60	53.3	104	39.0	189	26.9	176
120°28′E	Difference	+5.5	+4	+3.3	−26	+14.9	+20	+12.8	+15
2	T/P Crossover	13.4	140	5.3	78	44.9	201	22.5	165
5°58′S	ROMS	10.8	124	6.8	127	32.9	243	26.0	172
114°48′E	Difference	−2.6	−16	+1.5	+49	−12.0	+42	+3.5	+7
3	T/P Crossover	83.1	54	45.7	107	24.5	169	14.3	161
9°45′S	ROMS	92.9	60	52.5	105	39.5	185	23.4	171
119°3′E	Difference	+9.8	+6	+6.8	−2	+15.0	+16	+9.1	+10
4	T/P Crossover	84.7	62	56.6	124	40.1	193	23.2	182
13°30′S	ROMS	68.1	31	42.2	85	63.4	208	42.2	185
126°8′E	Difference	−16.6	−31	−14.4	−39	+23.3	+15	+15.0	+3
5	T/P Crossover	46.4	277	32.4	326	22.1	155	16.2	116
2°9′S	ROMS	43.3	289	27.3	336	20.8	143	21.8	129
119°3′E	Difference	−3.1	+12	−5.1	+10	−1.3	−12	+5.6	+13
6	T/P Crossover	62.2	120	24.1	167	29.9	184	19.2	172
9°45′S	ROMS	49.7	122	25.1	173	41.2	200	30.2	178
127°33′E	Difference	+12.5	+2	+1.0	+6	+11.3	+16	+11.0	+6
7	T/P Crossover	58.9	290	34.4	334	17.9	133	13.4	116
2°9′N	ROMS	61.7	292	33.7	339	18.7	95	14.3	124
120°28′E	Difference	+2.8	+2	−0.7	+5	+0.8	−38	+0.9	+8
8	T/P Crossover	43.5	189	14.2	252	26.6	230	26.4	217
9°46′S	ROMS	91.2	188	47.1	247	51.6	218	40.2	187
133°13′E	Difference	+47.7	−1	+32.9	−5	+25.0	+12	+13.8	−30
9	T/P Crossover	57.2	291	32.8	334	17.3	127	12.8	112
2°2′N	ROMS	58.9	293	31.4	338	18.0	116	15.8	106
123°17′E	Difference	+1.7	+2	−1.4	+4	+0.7	−11	+3.0	−6
10	T/P Crossover	25.6	160	11.0	249	21.8	170	14.2	155
2°3′S	ROMS	24.4	157	13.7	217	21.9	159	16.8	145
127°33′E	Difference	−1.2	−3	+2.7	−32	+0.1	−11	+2.6	−10
11	T/P Crossover	58.5	139	18.5	199	27.7	187	18.6	174
5°54′S	ROMS	52.5	150	27.5	207	38.1	196	28.5	172
131°49′E	Difference	−6.0	+11	+5.0	+8	+11.6	+9	+9.9	−2
12	T/P Crossover	59.6	290	33.1	334	17.6	135	13.5	117
5°56′N	ROMS	59.9	294	31.2	339	16.0	100	13.8	99
121°53′E	Difference	+0.3	+4	−1.9	+5	−1.6	−35	+0.3	−18
13	T/P Crossover	49.3	288	21.4	318	19.2	87	12.9	175
2°1′N	ROMS	40.7	275	18.0	314	35.5	63	19.9	25
128°58′E	Difference	−9.3	−13	−3.4	−4	+16.3	−24	+7.0	−150
	RMS All points	15.1	12	10.7	21	13.2	24	9.3	43
	RMS Excluding Site 8	7.6	12	5.8	22	11.7	24	8.8	44

[a]T/P is TOPEX/POSEIDON. Differences in amplitude and phase between the model estimate and the observation are given for each location. The RMS of the differences are listed at the bottom for all points and when site 8 and sites 8 and 10 are excluded.

[21] Baroclinic tides propagating along the track will have a coherent phase which increases or decreases along the track according to the propagation. If the propagation is directly along the track, the phase should vary smoothly. If it propagates, directly across the track, the phase will be constant for that section of the track.

[22] Two examples of smoothly varying phase can be seen in descending track 7 between ~11.5° and ~10.5°S and between ~8° and ~6°S (Figure 3i) and in ascending track 7 between 0° and 1°S (Figure 3d). Although the estimate is noisy, the phase steadily decreases in the first (Figure 3j) and increases in the latter (Figure 3e) with distance northward along the track. The bottom topography in these regions is quite rough (Figures 3j and 3e for the descending and ascending tracks, respectively) and 5 cm (Figure 3h) baroclinic M_2 tides appear plausible for the descending track and 3 cm (Figure 3d) for the ascending track. As the angle of the baroclinic tidal propagation moves away from the track, the sections with coherent phases indicate propagation decay. Deviations in amplitude may be baroclinic tides propagating along a different angle, an effect of another process, or noise in the data. The 5 cm amplitudes (Figure 3h) between ~3° and ~4°N do not show a coherent phase changing along the track (Figure 3i) although the phase is relatively stable for that portion. The feature is ~110 km wide, which is typical for a M_2 baroclinic wavelength in this area. So its identification as a baroclinic tide is inconclusive; however, if it is a baroclinic tide, it is propagating across, not along the track. In other areas, such as ascending track 7 between 15° and 10°S, the baroclinic amplitudes are small, less than 2 cm (Figure 3d), and the phase (Figure 3d) is extremely noisy. It is unlikely there is significant baroclinic amplitude in this region and if there is, it is well camouflaged in the noise.

3.2. Tidal Velocities

[23] Tidal velocity observations originated from moorings placed by different groups in the Indonesian Seas. All available mooring data were used, even though data were collected at different times and velocities in the region are

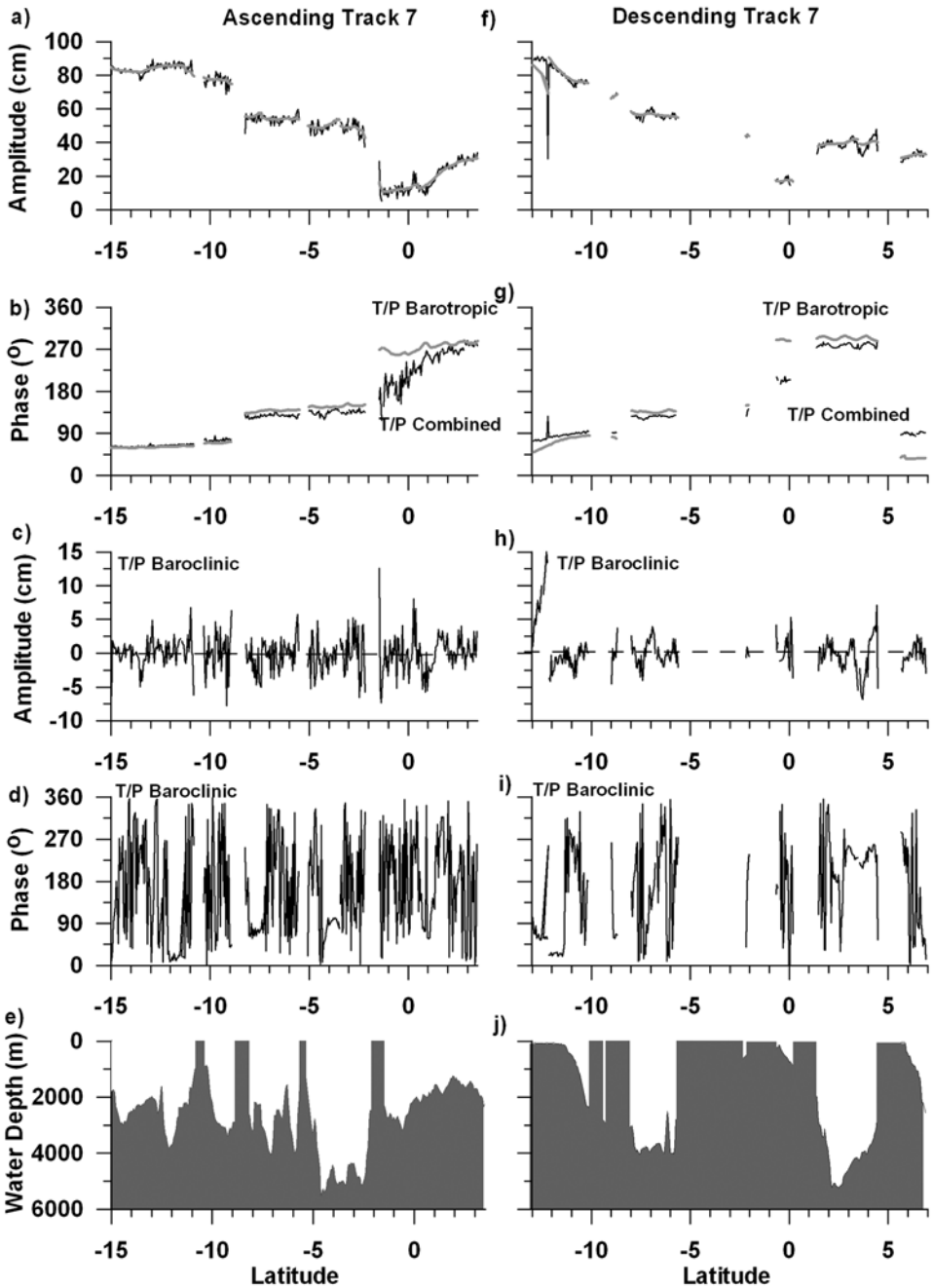

Figure 3. The (a) amplitude and (b) phase for M_2 from the TOPEX/POSEIDON along-track data for ascending track 7. The combined barotropic and baroclinic response is indicated by the black line and the barotropic response alone is indicated by the gray line. (c) The M_2 amplitude for the baroclinic response with zero indicated by a dashed line. (d) The M_2 phase for the baroclinic response is shown along with (e) the water depth along the track. (f–j) These variables are repeated for descending track 7.

dependent both on the seasons and El Niño/La Niña conditions [*Gordon*, 2005]. Most of these moorings have been deployed in straits or narrow passages, with two moorings in Makassar Strait, MAK-1 and MAK-2 [*Susanto et al.*, 2000] and one each in the Halmahera [*Cresswell and Luick*, 2001] and Maluku Seas [*Luick and Cresswell*, 2001] ((red) stars in Figure 1a). The instrument locations on the moorings are indicated by (red) diamonds in Figure 5.

[24] Current measurements obtained in these straits require careful analysis owing to mooring blowdown. These moorings were located in regions of very strong tidal currents, which were capable of pushing the mooring instruments down in the water column by as much as 200–300 m [*Susanto and Gordon*, 2005; *Molcard et al.*, 2001]. This resulted in both dropouts in the observations and the observations being collected at depths other than their target depth. The uppermost current meter on the western MAK-1 was near its target depth of 200 m for only 6% of the observation period [*Susanto and Gordon*, 2005]. The uppermost current meter on the eastern MAK-2

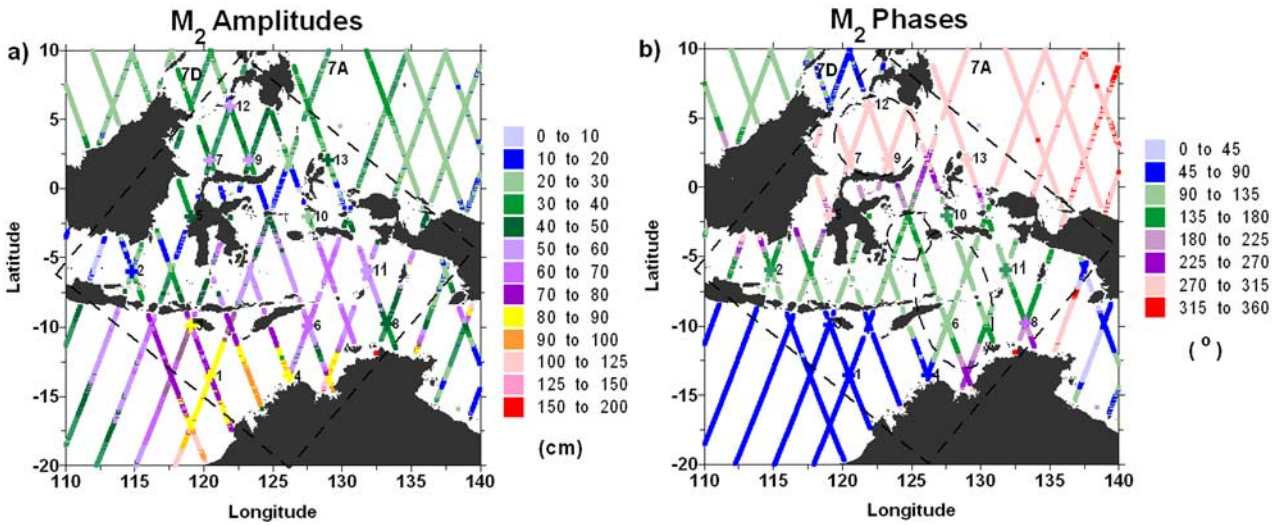

Figure 4. M_2 (a) phases determined from the along-track TOPEX/POSEIDON data using shaded coding for the values. Crossover data are indicated by plus signs using the same shaded coding with the location site labeled. (b) The circled areas are regions where strong internal waves in the elevation signal were indicated in the along-track observations. Ascending and descending tracks 7 are labeled as 7A and 7D, respectively.

was near its target depth of 205 m 32% of the time and the next lower instrument was near its target depth of 255 m 85% of the time [*Susanto and Gordon*, 2005]. Consequently, MAK-2 was more easily analyzed for tidal signals than MAK-1.

[25] To address the problem of the mooring depth fluctuations of tidal signals, time series data from the Makassar moorings, were analyzed using two different methods. (Published tidal results, not time series were used for the Halmerhera and Maluku Sea moorings.) First, sections without dropouts were analyzed using the T-tide tidal analysis software using the nominal depth of the instrument for the depth ((red) diamonds in Figure 5) with the uncertainties as determined by T-Tide shown as error bars [*Pawlowicz et al.*, 2002]. In the second method, time series were constructed at specific depths through the linearly vertical interpolation of the velocities based on depth according to the pressure gauge(s). Tidal analysis was performed on these constructed time series again using T-Tide. The major axes of the tidal ellipses for the constructed series are shown as (green) crosses in Figure 5 with the uncertainties given as error bars. The observed velocities varied with depth with the largest values in the upper water column. Owing to depression of the mooring by 200–300 m at times during deployment, there were no results above 50 m with the depth adjusted method. At Makassar mooring MAK-2, the two different methods performed similarly (Figures 5c and 5d); however, at MAK-1, they differed (Figures 5a and 5b). The depth adjusted observations peaked ~50 m deeper in the water column and the uncertainties were larger. There are some deficiencies with the method of adjusting for depth. There is no reason to believe that the velocities varied linearly between instruments or that linear interpolation provides a proper estimate of the velocity fields. Furthermore, the dropouts induced an additional bias in the measurements toward lower velocities, since the analysis was restricted to times without dropouts, i.e., lower velocities. Thus, the observations underestimated the tidal velocities especially in the upper water column, where dropouts were more frequent. Although there is no quantitative estimate of the underestimate, it is believed to be significant. Despite these caveats, the depth adjusted observations are likely to better estimate the observed tidal major axes than the original unadjusted observations.

4. Tidal Elevations

4.1. Tidal Elevation Fields

[26] The primary semidiurnal tidal components entered the region from the Indian Ocean, passing either through the Lombok Strait or Timor, Banda and Flores Seas into Makassar Strait (M_2 and S_2 shown in Figures 6c and 6g, respectively). Another component of the semidiurnal tides entered from the Pacific Ocean with the two components meeting in Makassar Strait and the Maluku and Halmahera Seas. The largest semidiurnal elevation amplitudes occurred along the Australian coast, in the Indian Ocean west of Timor, and in the Arafura Sea (M_2 and S_2 shown in Figures 6a and 6e, respectively), where M_2 amplitudes exceeded 75 cm. An amphidromic point formed in the Timor Sea. Elevation amplitudes ranged between 50 and 70 cm in the Sulawesi Sea, the northern portion of Makassar Strait, and parts of the Banda Sea and 70–90 cm in the Maluku Sea; otherwise, they were less than 50 cm, particularly in the Java Sea (M_2 shown in Figure 6a). Amplitudes in the Sulawesi, Maluku, Flores, and Banda Seas were modulated by the surface expression of the M_2 baroclinic tides as evidenced by the banding in these areas. The baroclinic tides in the Sulawesi Sea were particularly evident (Figure 6a). Typical length scales for these modulations were 100 km, which coincided with M_2 deep water baroclinic wavelengths.

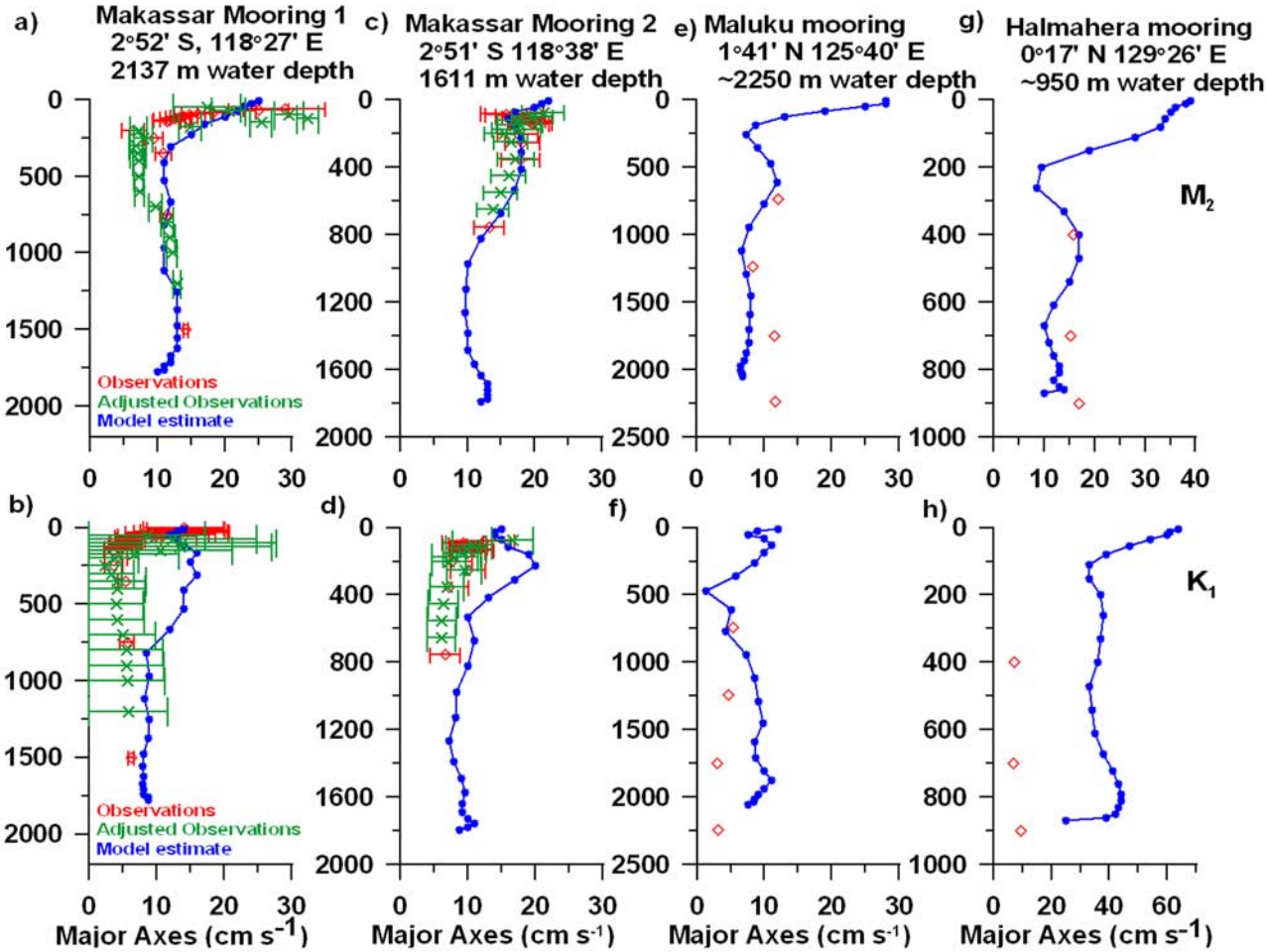

Figure 5. The M_2 major axes at the Makassar Strait Mooring (a) MAK-1 and (c) MAK-2 and (e) the Maluku mooring and (g) the Halmahera mooring are indicated by a line with dots at the levels for the model estimates, diamonds for the unadjusted observations, and crosses for the observations after adjustment for vertical mooring motion. The K_1 major axes at the Makassar Strait moorings (b) MAK-1 and (d) MAK-2 and (f) the Maluku mooring and (h) the Halmahera mooring using the same markings as for K_1. Observational uncertainties as determined by T-Tide are indicated by error bars, when available.

[27] Diurnal amplitudes were generally smaller and the progression simpler (K_1 amplitudes and phases in Figures 6b and 6d, respectively, and amplitudes and phases of O_1 in Figures 6f and 6h, respectively). The diurnal tides entered from the Pacific Ocean through the Sulawesi and Halmahera Seas into Makassar Strait, the Flores Sea, and Banda Seas and joined up in the Banda Sea and progressing through the Timor Sea into the Indian Ocean (K_1 in Figure 6d). The largest diurnal elevation amplitudes occurred along the Australian coast and between Australian and Papua/New Guinea, (K_1 in Figure 6b). Other than these regions and the Java Sea, amplitudes were less than 50 cm. An anomaly in the diurnal behavior occurred along the equator as a minimum in amplitude and an anomaly in phase. The K_1 amplitudes showed evidence of modulation by baroclinic tides particularly in the Sulawesi Sea, with wavelengths on the order of 200–300 km, which is consistent with typical diurnal internal wavelengths for deep water. Diurnal wavelengths are longer than those of semidiurnal tides in the corresponding water depth. The behaviors of the M_2 and K_1 tidal constituents were consistent with the 2-D inverse model of *Ray et al.* [2005].

4.2. Comparison to Available Data

4.2.1. T/P Crossover

[28] Thirteen T/P crossover locations fell within the model domain (Figure 2). Elevation amplitudes and phases at each location for each of the four tidal constituents from the T/P observations are given in Table 1, along with the corresponding model estimates at those locations and the differences between the model estimates and the observations. The semidiurnal constituents agreed within 10 cm with the T/P observations except at 3 (2) points for M_2 (S_2). The greatest amplitude differences occurred at site 8, which is near the Arafura Sea near the edge of the domain in a region with a high-amplitude gradient. Sites 4 and 6, which are near the amphidromic point, showed large differences in amplitude and also phase for site 4. Near an amphidromic point both the amplitude and phase change dramatically over small spatial scales and a small difference in either the

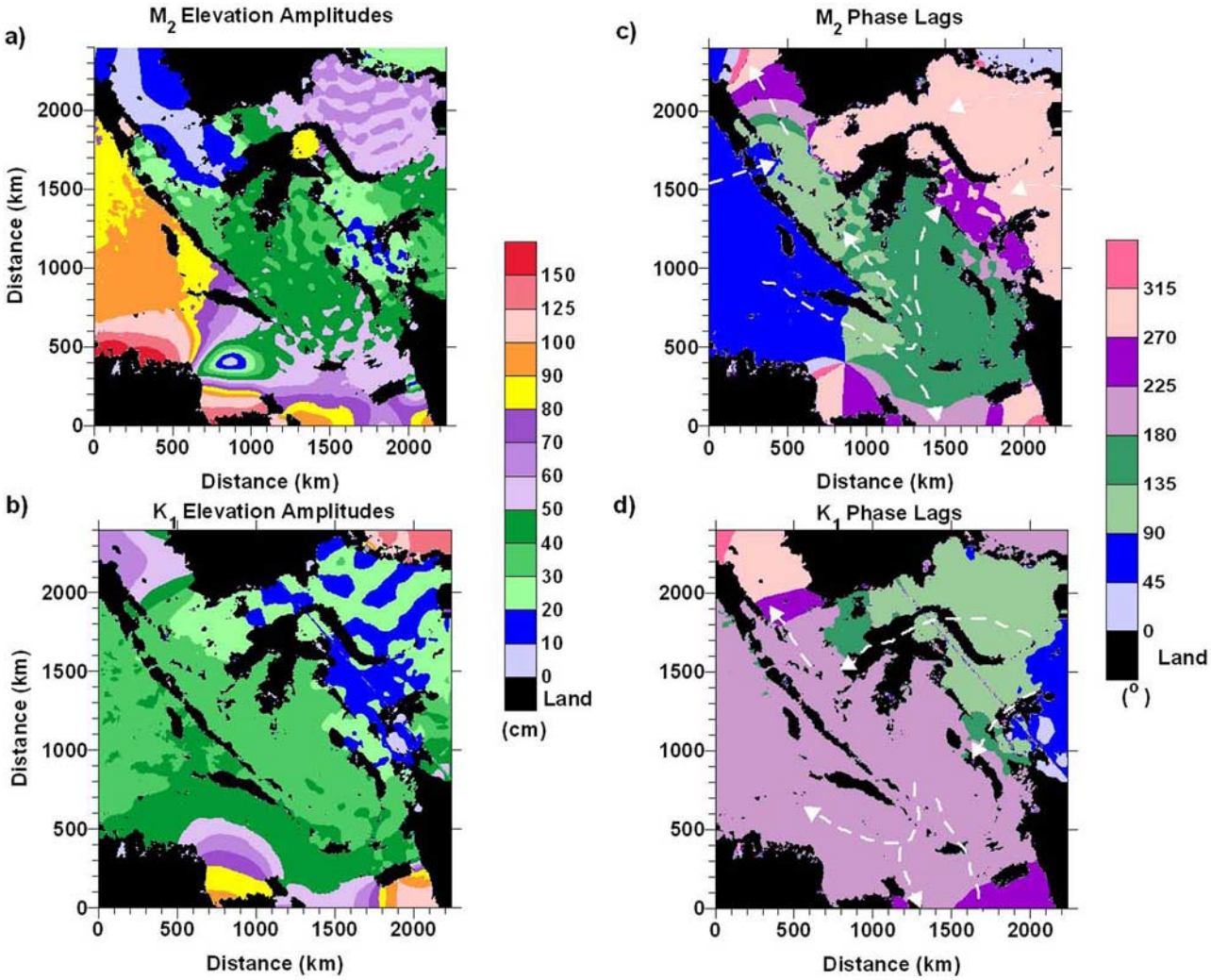

Figure 6. The elevation amplitude for the (a) M_2 and (b) K_1 tidal constituents over the model domain and the phases for (c) M_2 and (d) K_1. Propagation of the tides through the domain is indicated in Figures 6c and 6d by arrows. The elevation amplitude for the (e) S_2 and (f) O_1 tidal constituents over the model domain and the phases for (g) S_2 and (h) O_1. Propagation of the tides through the domain is indicated in Figures 6g and 6h by arrows.

observation or amphidromic point location can easily result in large differences in amplitude and phase. With the diurnals, sites 4 and 8 had the largest difference in amplitude and again they are located in areas with large gradients in the diurnal amplitudes. For the diurnal constituents, differences increased with passage through the domain, particularly after the Makassar Strait and the Banda Sea, so in the Java, Timor, and Arafura seas and the Indian Ocean. Generally, the largest differences between the model estimates and the observations occurred in areas with rapidly changing values.

[29] RMS differences between the model estimates and the observations for all locations were 15.1 cm for M_2, 10.7 cm for S_2, 13.2 cm for K_1, and 9.4 cm for O_1 for amplitude and 12° for M_2, 21° for S_2, 24° for K_1, and 43° for O_1 for phase. If site 8 is excluded, RMS differences were reduced to 7.6 cm for M_2, 5.8 cm for S_2, 11.7 cm for K_1, and 8.8 cm for O_1 for amplitude. There were no appreciable phase reductions. In general, the model performed better for the semidiurnal constituents than the diurnal constituents.

4.2.2. T/P Along-Track

[30] The combined barotropic and baroclinic along-track M_2 tidal elevation amplitudes and phases were compared to the model estimates (Figure 7). Generally, there were 10–20 cm differences in amplitude (Figures 7a and 7c) and 0–20° differences in phase (Figures 7b and 7d). This exceeds the standard error estimates for the observational data of 1 cm in amplitude [*Ray and Mitchum*, 1997]. Most of the discrepancies coincided with the differences between the crossover and the along-track estimates. Since the crossover estimates are believed to be more accurate, the along-track estimates appear to be sufficient only for a qualitative comparison. It is interesting to note that where the along-track estimates have features in amplitude with spatial scales on the order of 100–150 km, such as between 8°S and 6°S and 1°N and 4°N in descending line 7 (Figure 7c) and between 0°N and 3°N in ascending line 7 (Figure 7a), the model also shows modulation of the elevation amplitude on the same spatial scales. As discussed in section 4.1, these modulations in amplitude are the surface expressions of the

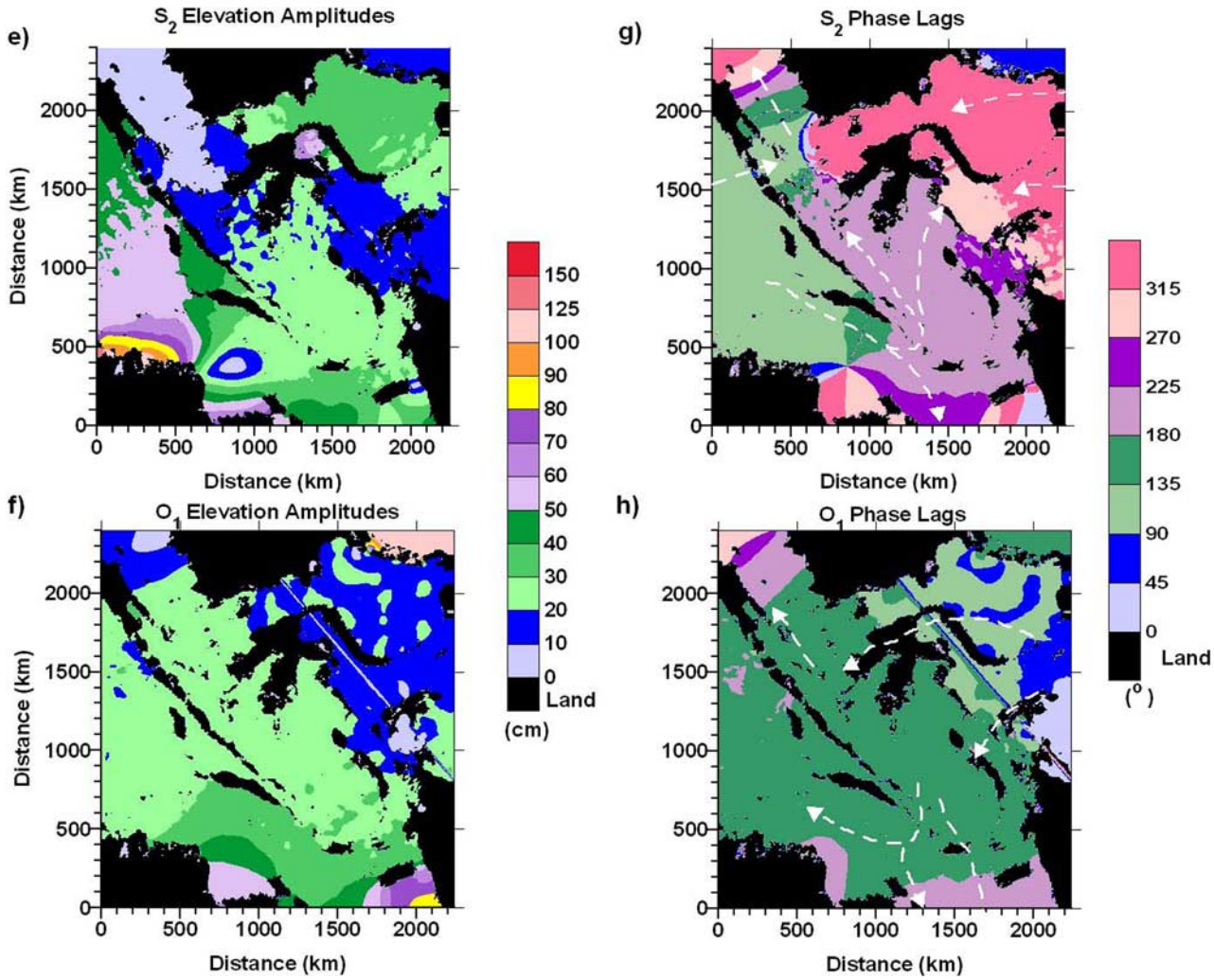

Figure 6. (continued)

baroclinic tides. Analysis of all the tracks indicated that M_2 baroclinic tides were generated in the Sulawesi, Maluku, Banda, and Flores Seas (circled regions in Figure 4b). These agreed well with the model estimates for regions with surface modulations indicating M_2 baroclinic tides (Figure 6a). Thus, a positive qualitative evaluation was obtained, even though the quantitative evaluation was not optimal.

4.2.3. Sources of Model Error

[31] There are four key factors in these simulations: topography, stratification, resolution, and tidal forcing. *Smith and Sandwell* [1997] topography was used for these simulations and is probably the largest source of error in these simulations. Basically, the topography of the Indonesian Seas is still not well known at a resolution of 5 km. This was a contributing factor to not pursuing higher-resolution simulations. Improvements are being made in topographic data and more accurate bathymetry has become available since the study was commenced, for example the ETOPO-2 [*National Geophysical Data Center*, 2001] data set with a resolution of 0.033° in latitude (~2 km) and longitude. Stratification is key in internal wave generation and errors in the initial stratification are probably the second largest source of error in the model results. The model stratification was generated from averages of observed temperature and salinity profiles over a grid with 0.1° spacing. Unfortunately, the grid was not completely filled. Furthermore, the profiles in the cells were often collected in different seasons, resulting in a patchwork of regional biases through the stratification. As more hydrographic data are obtained, better estimates of the stratification will improve. Higher resolution improves model performance and a 5 km resolution is barely sufficient for simulating internal tides [*Robertson*, 2006]. The tidal forcing is also key, but is the best known and best constrained of these three factors. The tidal coefficients taken from *Egbert and Erofeeva*'s [2002] global inverse tidal model (OTIS) are constrained against years of TOPEX/POSEIDON and tidal gauge data and are considered one of the most accurate tidal elevation estimates [*Anderson et al.*, 1995]. Other sources of error also exist in the model dynamics and physical processes, which are not included in or resolved by the model. Wind, solar radiation, and dynamic height differences have not been included, as this was a study of tides. However, they generate mean currents which interact with and affect the tides, modifying the results. Here, we investigated tidal dynamics in the

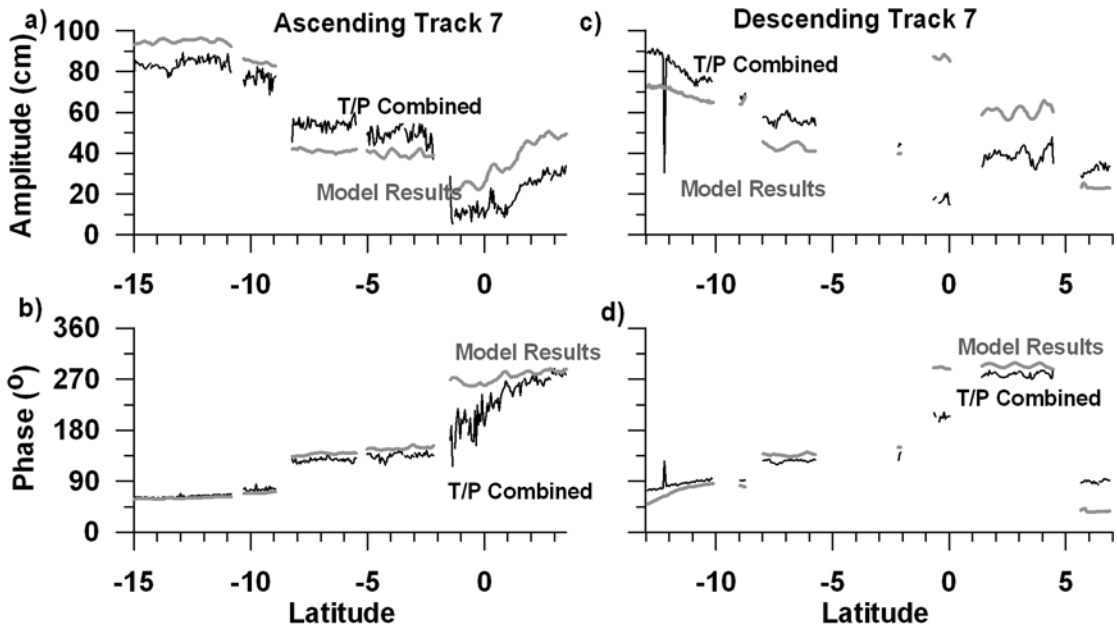

Figure 7. Comparison of the (a) amplitude and (b) phase for M_2 from the TOPEX/POSEIDON along-track data for ascending track 7 (black lines) with model estimates for those locations (gray lines). (c, d) The corresponding data for descending track 7.

region with the best available topography, stratification, and tidal forcing.

5. Tidal Velocities

[32] Depth-independent and depth-dependent velocities were generated by the model from the 2-D and 3-D modes, respectively. The depth-dependent velocity represents the complete velocity at each level and is not a perturbation from the vertical mean. Although the depth-independent and depth-dependent velocities are linked in the model, the average of the depth-dependent velocity over the water column may differ slightly from the depth-independent value. Baroclinic anomaly velocities were calculated and represent the difference between the depth-dependent and depth-independent velocities.

5.1. Tidal Velocity Fields

[33] Time series of both depth-independent and depth-dependent velocities and baroclinic anomalies were tidally analyzed using *Foreman*'s [1978] software for the tidal ellipse parameters: major and minor axes, inclination, and phase.

5.1.1. Depth-Independent Velocities

[34] Depth-independent tidal velocities were small, <10 cm s^{-1}, over most of the region, as evidenced by the major axes of the tidal ellipses for both the semidiurnal and diurnal constituents (M_2 for semidiurnal in Figure 8a and K_1 for diurnal in Figure 8d). However, high velocities, exceeding 50 cm s^{-1}, occurred in narrow straits between islands, such as Lombok Strait, and over parts of the continental shelf along Australia (Figures 8a and 8d). Depth-independent velocities were strongly correlated with topography with higher values in the shallow coastal regions and low values, <2 cm s^{-1} in the deeper water midbasin.

5.1.2. Depth-Dependent Velocities

[35] Depth-dependent tidal velocities showed higher variability than depth-independent velocities (Figures 8a and 8d for M_2 and K_1, respectively), as seen in the maximum major axes of the tidal ellipses for the semidiurnal (M_2 in Figure 8b) and diurnal (K_1 in Figure 8e) constituents. Again, velocities were generally larger in shallow water and smaller in the deep basins. However, even in the deep basins, major axes commonly exceeded 10 cm s^{-1} (Figures 8b and 8e). To determine the increase in the depth-dependent velocities over the depth-independent velocity, the baroclinic anomaly attributable to each constituent was determined by differencing the major axes of the depth-dependent and the depth-independent velocities, thereby isolating the anomalies associated with the constituent. Except in shallow regions, the maximum baroclinic anomaly for the M_2 and K_1 constituents (Figures 8c and 8f, for M_2 and K_1, respectively) generally exceeded 5 cm s^{-1} and often exceeded 10 cm s^{-1}. In narrow straits and parts of Ceram and Halmahera Seas, the maximum baroclinic anomalies were higher, 30–50 cm s^{-1}, particularly for K_1. Thus, except in shallow water, baroclinic velocities generally exceeded the barotropic tidal velocities.

[36] The baroclinic response was quite complex spatially, both in horizontal and vertical directions. All four constituents were strongly depth-dependent, particularly in straits and near rough topography, indicating active internal tide generation and propagation. Like finestructure in the observations [*Ffield and Robertson*, 2006, 2008], this internal tidal activity was larger and more intense near topographic features. In general, beams of internal tides appeared to originate over sills and ridges from the bottom and follow the path of a typical internal wave ray (Figure 9). Other beams originated near the surface and either were surface trapped or propagated deeper in the water column. Owing to

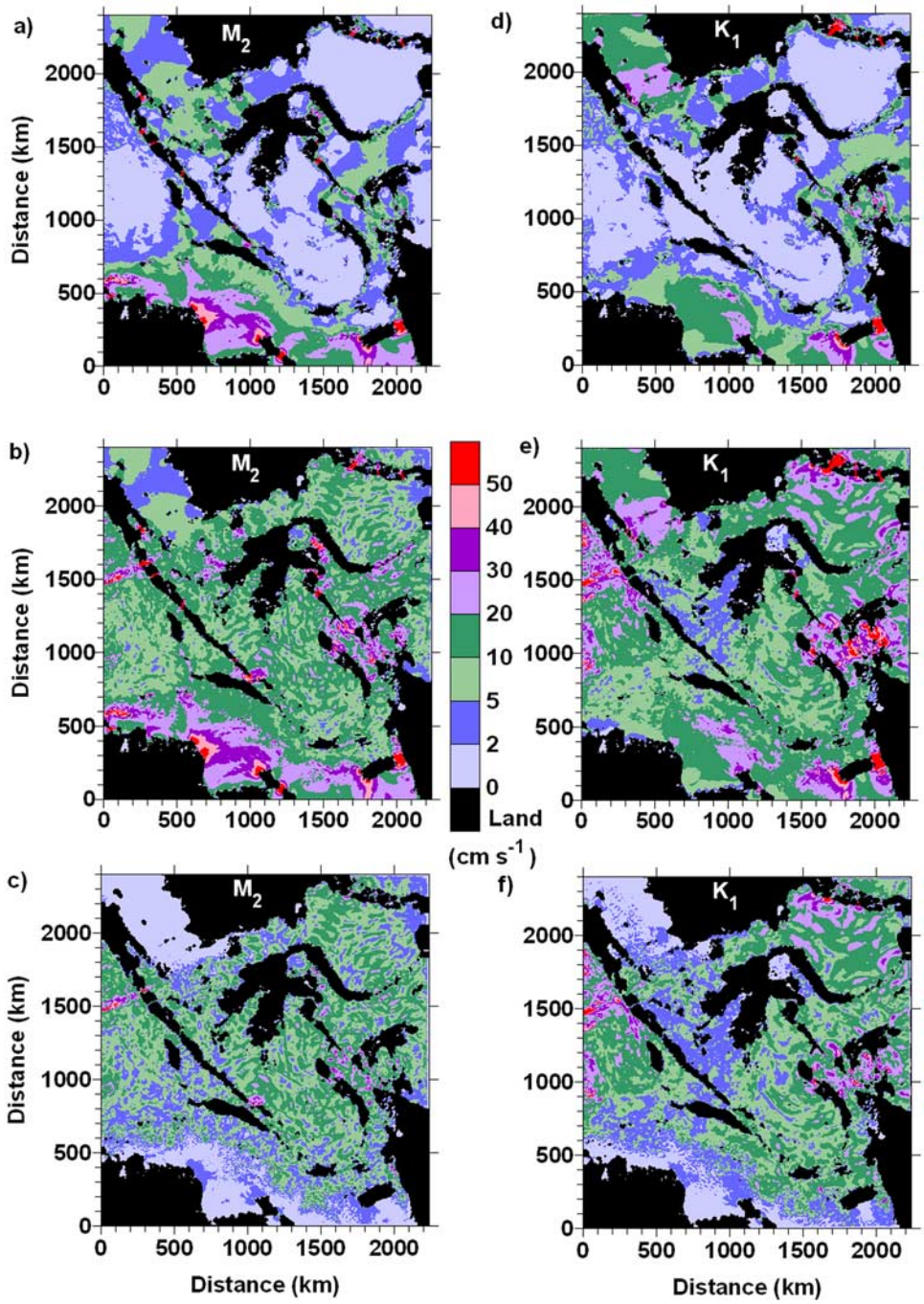

Figure 8. Amplitudes of the major axis of the (a) M_2 and (d) K_1 tidal ellipses from the depth-independent velocities. The maximum depth-dependent major axes in the water column at each grid cell of the (b) M_2 and (e) K_1 tidal ellipses. The maximum baroclinic anomaly for (c) M_2 and (f) K_1, with the baroclinic anomaly defined as the difference between the depth-independent and maximum depth-dependent major axes.

the narrowness of many of the channels and features, beams seldom propagated in isolation, but interacted with beams generated by nearby topographic features, such as a ridge or the other side of a channel, or with beams propagating from other directions. Even in rare cases with an isolated single beam, it interacted with reflections of itself from the surface or bottom. These interactions occurred not only between internal tides at the same frequency, but also between different constituents. Interactions between internal tidal beams of one constituent are discussed in this paper; however, interactions between different tidal constituents are discussed in a companion paper (Robertson and Ffield, submitted manuscript, 2008).

[37] It is beyond the scope of this paper to cover the intricacies of the internal tides for the entirety of the Indonesian Seas. Five transects were selected in regions believed to be major passages or locations of intense mixing [*Gordon et al.*, 2006; *Koch-Larrouy et al.*, 2007] to show

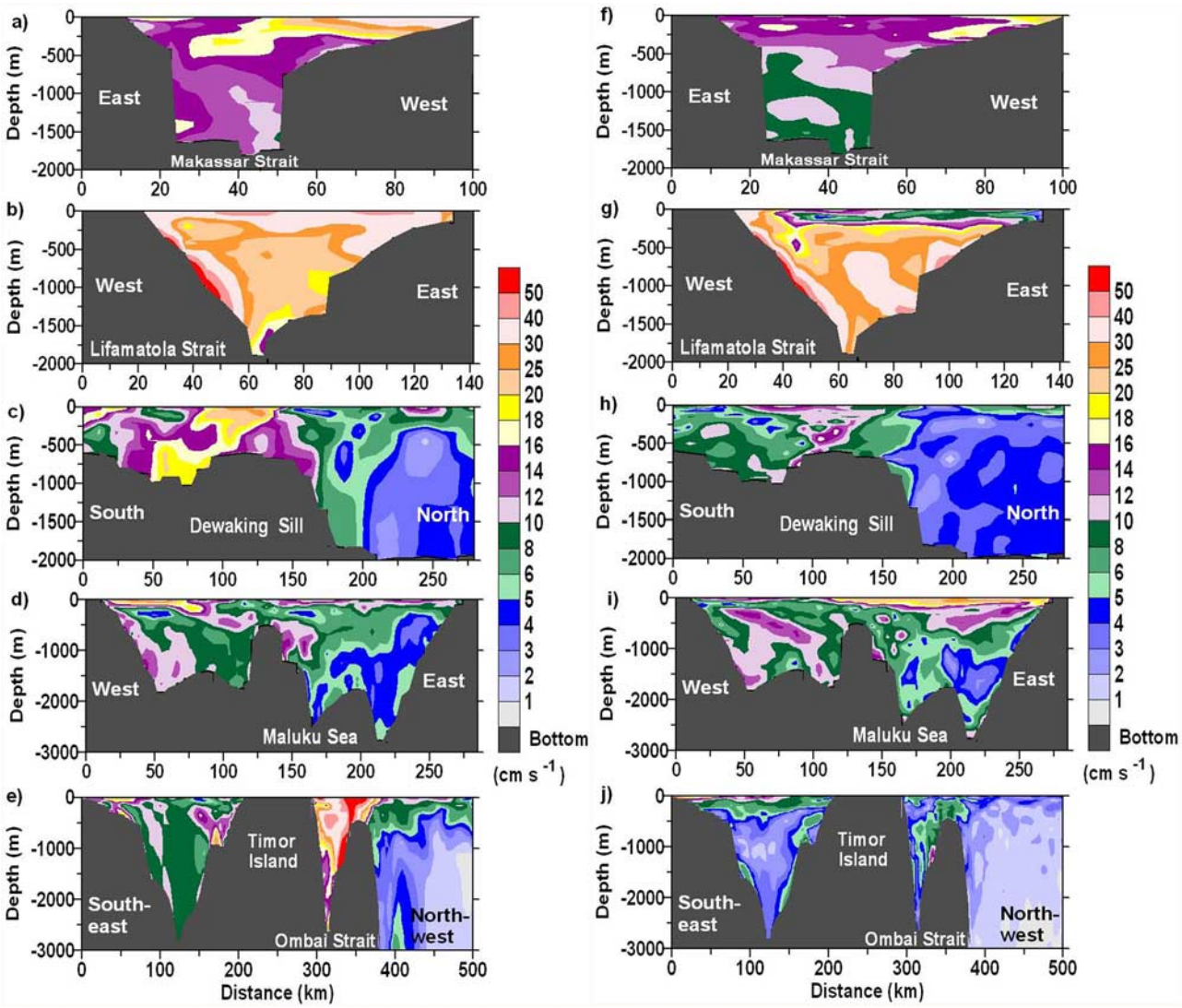

Figure 9. Transects of the major axes of the M_2 tidal ellipses from the depth-dependent velocities for (a) Makassar Strait, (b) Lifamatola Strait, (c) over Dewakang Sill, (d) Maluku Strait, and (e) Timor and Ombai straits. Transects of the major axes of the K_1 tidal ellipses from the depth-dependent velocities for (f) Makassar Strait, (g) Lifamatola Strait, (h) over Dewakang Sill, (i) Maluku Strait, and (j) Timor and Ombai straits. Transects of the major axes of the S_2 tidal ellipses from the depth-dependent velocities for (k) Makassar Strait, (l) Lifamatola Strait, (m) over Dewakang Sill, (n) Maluku Strait, and (o) Timor and Ombai Straits. Transects of the major axes of the O_1 tidal ellipses from the depth-dependent velocities for (p) Makassar Strait, (q) Lifamatola Strait, (r) over Dewakang Sill, (s) Maluku Strait, and (t) Timor and Ombai Straits.

baroclinic tidal responses for these regions of interest (transect locations shown in Figure 1b). Major axes (Figure 9) and phases (Figure 10) of the tidal ellipses were calculated from the depth-dependent velocities along these transects. The selected transects were in regions with strong tidal currents (Figures 8a and 8d for the M_2 and K_1 constituents, respectively). Various baroclinic responses can be seen in these selected transects dependent on the bathymetric and stratification conditions. As semidiurnal responses were quite similar to each other M_2 was selected to represent the semidiurnal response (Figures 9a–9e). Likewise the diurnal responses were quite similar to each other and K_1 was selected to represent the diurnal response (Figures 9f–9j). Major axes and phases for S_2 are shown in Figures 9k–9o and Figures 10k–10o, respectively, and those for O_1 are shown in Figures 9p–9t and Figures 10p–10t, respectively. It should be noted that internal wave rays radiate in different directions from bathymetric features and these 2-D transects cut along some of the internal wave rays and across others. Thus in the transect, only a cross-beam footprint of an internal tidal beams may be evident. To address this, 3-D images of the M_2 and K_1 major axes of the region surrounding the transects have been included as auxiliary material[1].

[1]Auxiliary materials are available in the HTML. doi:10.1029/2007JC004677.

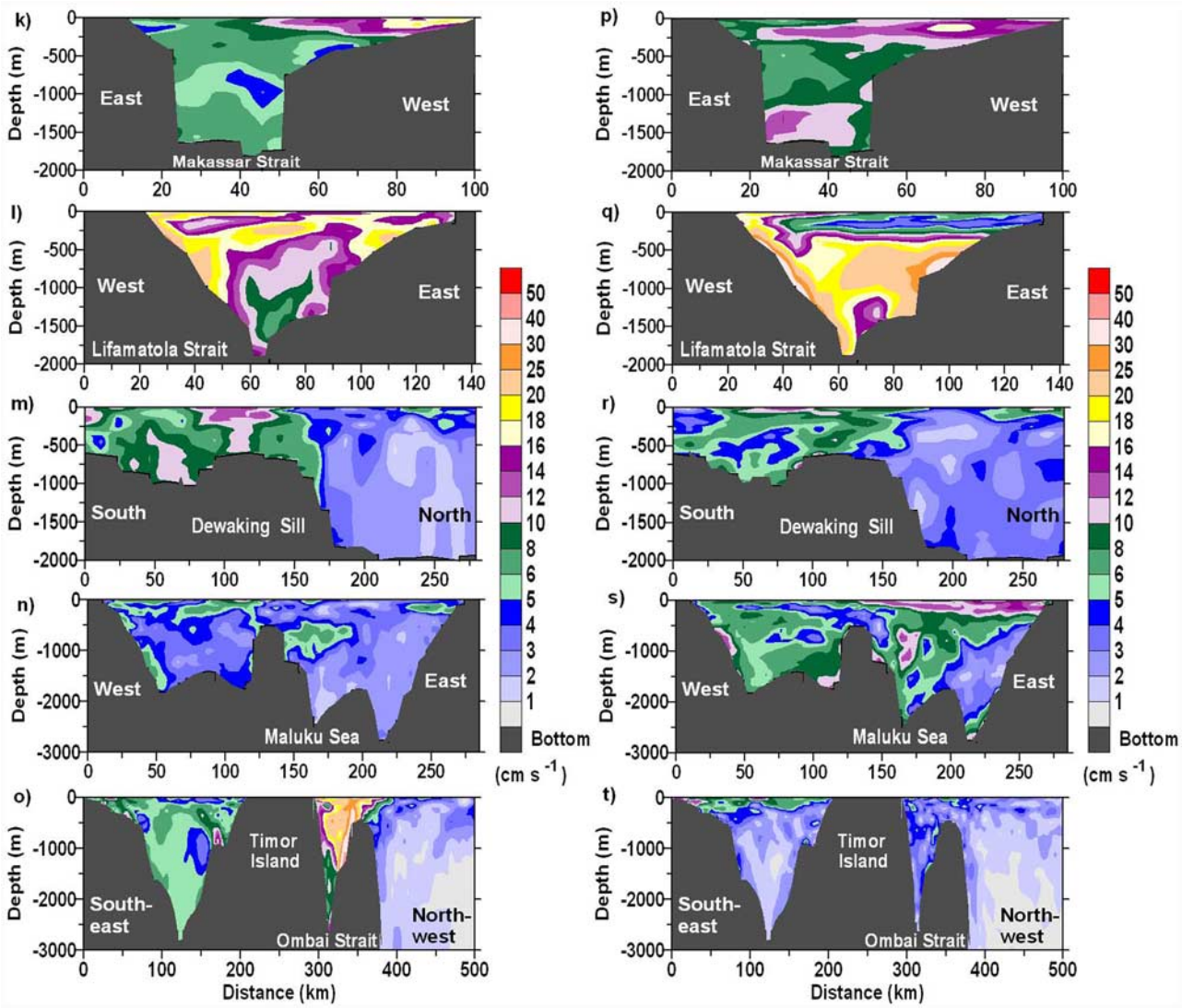

Figure 9. (continued)

[38] M_2 tides from the Pacific and Indian oceans converge south of Makassar Strait and one transect crossed through Makassar Strait, roughly 300 km from this convergence. Along this transect, M_2 elevation amplitudes were ~30 cm with a considerable cross-transect gradient (Figure 6a). K_1 elevation amplitudes were smaller, ~20 cm, with less of a spatial gradient (Figure 6b). Barotropic (depth-independent) M_2 major axes increased from 10 to 20 cm s^{-1} on the eastern side reaching 30–40 cm s^{-1} toward the western side (Figure 8a). Barotropic (depth-independent) K_1 major axes ranged from 10 to 20 cm s^{-1} (Figure 8d). The M_2 depth-dependent major axes agreed with typical values of 10–16 cm s^{-1} through most of the transect exceeding over 30 cm s^{-1} near the surface in the shallow western region (Figure 9a). K_1 depth-dependent major axes were smaller, typically ~14 cm s^{-1} above 700 m and 8–12 cm s^{-1} below 700 m (Figure 9f). A strong beam of M_2 tidal energy originated in the shallow water on the western side of the strait near the surface (Figure 9a) with the phase indicating propagation deeper into the water column and eastward along the transect (Figure 10a), which is consistent with upward energy propagation. The beams of peak major axes roughly followed the internal wave ray characteristic slope. The 3-D images of the major axes for the region (available in the auxiliary material) showed multiple beams emanating from the shallow regions on the western side and propagated in different directions. Two other M_2 internal tide beams originated at the bottom on the western side of the strait at roughly 700 m and 1700 m depth. In contrast to the surface M_2 tidal beam, these benthic beams opposed the barotropic M_2 tide and interacted destructively, reducing the major axis (Figure 9a). A surface internal tide beam also originated from the west side for the K_1 constituent (Figure 9f) and the phase shows it propagated eastward across the strait both along the surface and deeper into the water column (Figure 10f and the 3-D image). Although it was not as strong as the M_2 surface beam (Figure 9f), it interacted constructively with the barotropic tide. In addition, there were two benthic K_1 internal tidal beams, one originating on the east side at about 1600 m and one on the west side at about 1000 m. The two benthic beams originated off transect, propagating through the transect (3-D image) and

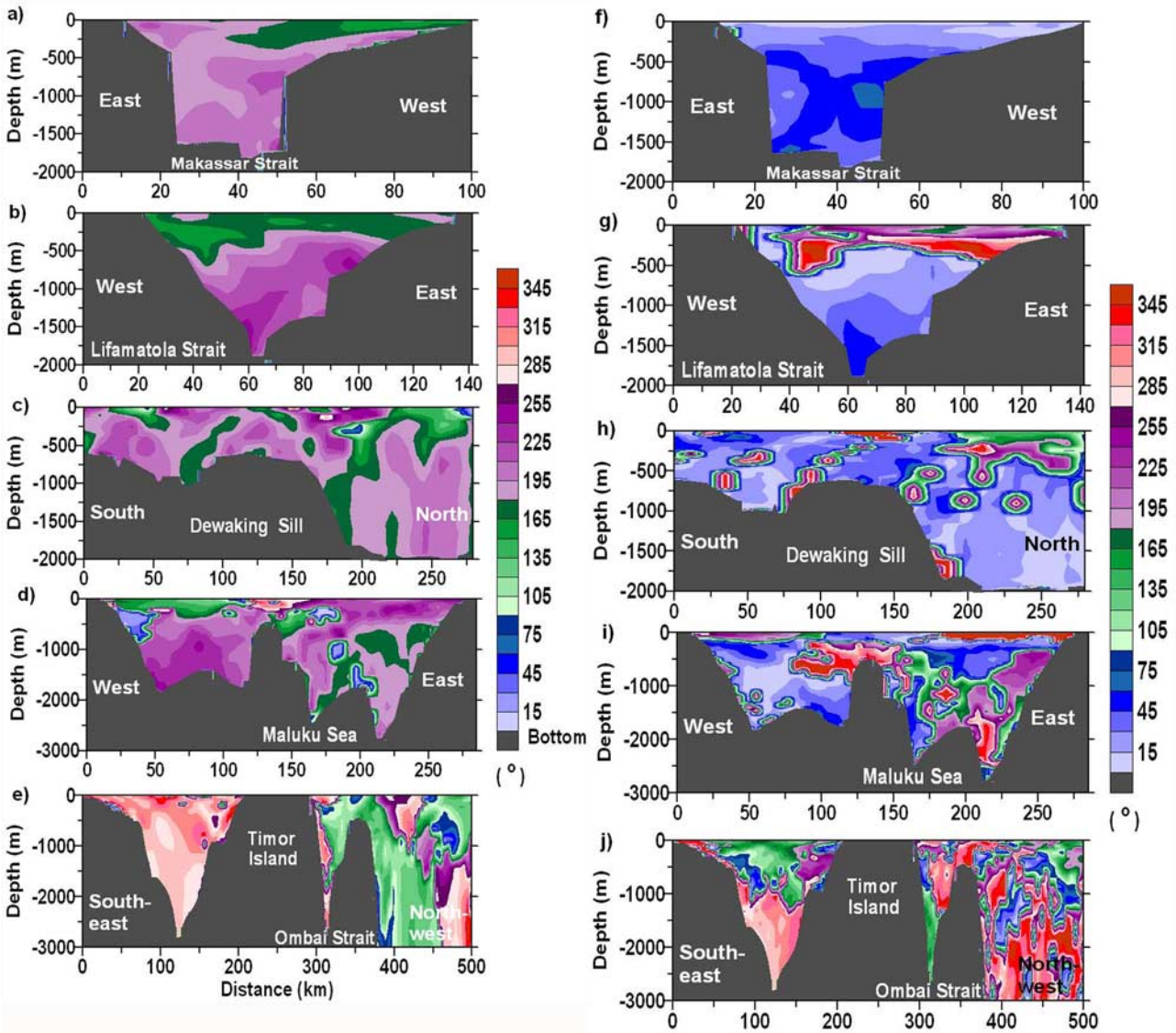

Figure 10. Transects of the phases of the M_2 tidal ellipses from the depth-dependent velocities for (a) Makassar Strait, (b) Lifamatola Strait, (c) Maluku Strait, (d) over Dewakang Sill, and (e) Timor and Ombai straits. Transects of the phases of the K_1 tidal ellipses from the depth-dependent velocities for (f) Makassar Strait, (g) Lifamatola Strait, (h) Maluku Strait, (i) over Dewakang Sill, and (j) Timor and Ombai straits. Transects of the phases of the S_2 tidal ellipses from the depth-dependent velocities for (k) Makassar Strait, (l) Lifamatola Strait, (m) Maluku Strait, (n) over Dewakang Sill, and (o) Timor and Ombai Straits. Transects of the phases of the O_1 tidal ellipses from the depth-dependent velocities for (p) Makassar Strait, (q) Lifamatola Strait, (r) Maluku Strait, (s) over Dewakang Sill, and (t) Timor and Ombai Straits.

appeared to interfere destructively with the K_1 surface beam.

[39] Effects of destructive interference were also clear in a transect in Lifamatola Strait. Lifamatola Strait is in a confluence region for the M_2 tides coming from the Indian and Pacific Ocean and also the K_1 tides coming through Makassar Strait and the Maluku Sea (Figures 6c and 6d for M_2 and K_1, respectively). Tidal elevation amplitudes were small for both constituents 10–30 cm (Figures 6a and 6b for M_2 and K_1, respectively). However, barotropic velocities were high, 30–50 cm s^{-1} for all four tidal constituents (Figures 8a and 8d for M_2 and K_1, respectively). Depth-dependent major axes were also high, with beams of low values on the eastern side near the bottom for M_2 (Figure 9b) and at the surface for K_1 (Figure 9g). These low-value beams indicate opposition between the barotropic and baroclinic tidal currents. At first glance it appeared that an M_2 internal tidal beam originated on the east side at ~1000 m (Figure 9b). However, inspection of the phase showed that two M_2 benthic beams formed, one on the east side at ~700 m and one on the west side at 1500 m (Figure 10b). Both beams opposed the barotropic tidal currents. They interacted with each other constructively, but destructively with the barotropic tide decreasing its flow

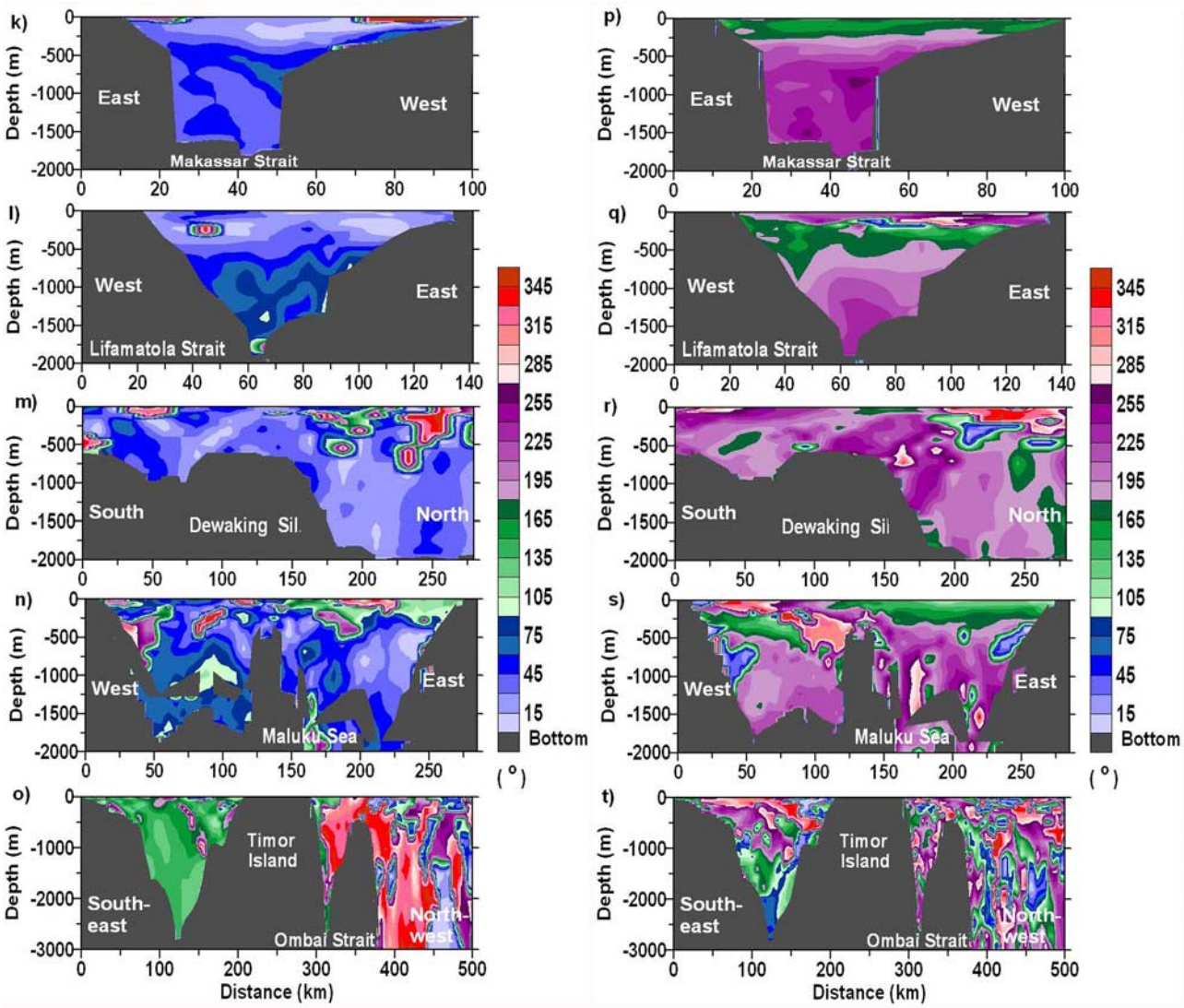

Figure 10. (continued)

on the eastern side at the bottom of the trench and at ~800 m (Figure 9b). The prominent feature in the K_1 major axes was the strong surface maximum extending from the eastern side over much of the domain (Figure 9g). The 3-D images of the M_2 major axes for the region (included in the auxiliary material) showed a strong beam of tidal major axes was generated northeast of the transect and propagated through it. This beam interacted destructively with the barotropic tide, reducing its strength and resulting in a strong surface minimum. Interference also occurred near the surface, in the western portion of the transect, modifying the K_1 major axes and phase (Figure 10g). Inspection of the 3-D image of the K_1 major axes (included in the auxiliary material) indicated intersections of baroclinic activity within the strait and entering the transect from the surrounding region.

[40] Makassar Strait is a major transit area for water flowing through the Indonesian Sea. Dewakang Sill lies just south of Makassar Strait and has been postulated to be a source of tidal mixing [*Koch-Larrouy et al.*, 2007]. A transect was selected across the sill roughly along the predominant flow direction to investigate this mixing and the baroclinic tides (Figure 1b). Along this transect, elevation amplitudes were small, <20 cm for M_2 (Figure 6a) and ~20–30 cm for K_1 (Figure 6b). Barotropic (depth-independent) tidal velocities ranged from 2 to 30 cm s^{-1} for M_2 and from 2 to 20 cm s^{-1} for K_1 (Figures 8a and 8d, respectively) peaking over the sill, particularly for M_2. The baroclinic response was quite active for both the M_2 and K_1 constituents, particularly south of the sill (Figures 9c and 9h, respectively). M_2 internal tidal beams radiated from the south side of the sill across the transect (Figures 9c and 10c for major axes and phases, respectively). The 3-D image of the major axes (included in the auxiliary material) indicated the beams propagated across not along the transect. Again these beams followed the characteristic slope for an internal wave ray characteristic for this stratification and these frequencies. Peak values in M_2 occurred at the surface and some beam intersection locations. Reflection from the surface and changes in propagation speed also contributed to these peak surface values. Gradients in the M_2 major axes were quite strong, imparting high vertical shear in the horizontal velocities of this region. Similarly, internal tide

beams for K_1 were generated off transect (Figure 9h) and propagated through the transect (Figure 10h), although they were not as strong as the M_2 beams (Figure 9c). The phase diagram showed some propagation along these beams, but over most of the transect, the phase was constant, indicating cross-transect propagation (Figure 10h). This was confirmed in the 3-D images (included in the auxiliary material), which showed cross-transect propagation. This intense internal tidal activity over Dewaking Sill supports the active mixing of *Koch-Larrouy et al.*'s [2007] mixing model study.

[41] Both M_2 and K_1 tides propagated from the Pacific Ocean through the Maluku Sea and across its transect (location shown in Figure 1b). Tidal elevation amplitudes along the transect were relatively small 20–30 cm for M_2 and 10–20 cm for K_1 (Figures 6a and 6b, respectively). Barotropic tidal velocities were fairly uniform along the transect, between 5 and 10 cm s^{-1} (Figures 8a and 8d for M_2 and K_1, respectively). In contrast, the depth-dependent major axes ranged from 2 to 40 cm s^{-1}, for both tidal constituents (Figures 9d and 9i for M_2 and K_1, respectively). Like Dewaking Sill, the 3-D image (included in the auxiliary material) showed tidal beams generated off transect propagating through the transect. The peak M_2 major axis occurred on the western side and appeared be surface trapped (Figure 9d for major axes and Figure 10d for phase). There was also a surface-trapped beam propagating along the transect from the eastern side for K_1 (Figure 9i for the major axis and Figure 10i for phase). A K_1 internal tidal beam originated from the upper water column on the west side and propagated deeper into the water column (Figure 9i). In the eastern portion of the transect, the picture was extremely complex. The 3-D images for K_1 (included in the auxiliary material) indicated generation of multiple beams with some beams propagating in various directions. Again, both constructive and destructive interference occurred between the beams obscuring clean ray patterns and resulting in complex, sharp gradients in the major axes for the depth-dependent velocities, even though the region did not have the large major axes of Makassar or Lifamatola straits.

[42] The Timor Sea and Ombai Strait are major transport routes of the Indonesian Throughflow [*Gordon*, 2005; *Molcard et al.*, 2001]. The final transect passed from the continental shelf off Australia through the Timor Sea and Ombai Strait into the Flores Sea (Figure 1b). Tidal elevations were similar and quite high, <50 cm, for both M_2 and K_1 in the Timor Sea and Ombai Strait; however, northwest of Ombai Strait in the Flores Sea, the tide had a different phase, since it is in a different stage of propagation, and tidal elevations were smaller (Figure 6). Barotropic tidal velocities were quite low, <5 cm s^{-1} in the Flores Sea for both constituents and only slightly higher, <10 cm $s^{-1}$for K_1 in the Timor Sea and Ombai Strait; however, M_2 barotropic tidal velocities were higher in the Timor Sea, >10 cm s^{-1}, and quite large in Ombai Strait >50 cm s^{-1} (Figures 8b and 8e for M_2 and K_1, respectively). Likewise, there was more internal tidal activity for M_2 than for K_1 in Ombai Strait (Figures 9e and 9j for M_2 and K_1, respectively). K_1 was more active over the Australian continental slope and shelf than in Ombai Strait. Strong M_2 internal tidal beams originated from the northwest side of Ombai Strait and the southeast side of Timor Island (Figure 9e). At both of these sites propagation occurred both into the strait or sea and up the slope parallel to but slightly above the bottom for all constituents. An example of this slope following beam is clearly seen for M_2 as it continued to propagate through the upper water column reaching the surface above the sill northwest of Ombai Strait (Figure 9e for the major axis and Figure 10e for the phase). Another M_2 internal tidal beam originated at ~500 m on the northwest side of the sill, propagating northwest into the Flores Sea, undergoing reflection from the surface as it propagates (Figure 9e for the major axis and Figure10e for the phase). This generation appeared localized to a region ~50 km in the x direction and 100 km in the y direction (3-D image included in the auxiliary material). The beams did not propagate directly along the transect, but at an angle with it. Additionally, M_2 internal tides were generated at the Australian continental shelf/slope break (Figure 9e) with phase propagating both along the bottom and at the surface (Figure 10e). K_1 internal tides were strongest along the Australian continental shelf/slope break (Figure 9j), and surface trapped (Figure 10j). Beams of K_1 internal tides were also generated on the northwest side of Ombai Strait at ~1200 m and the top of the sill (Figure 9j). In Timor Sea, the phase indicated that there are two different regimes with the K_1 internal waves with the boundary roughly along the 1000 m isobath (Figure 10j) and the smallest major axes at this depth (Figure 9j). There was some indication of bottom generated signals below 1000 m on both sides of the channel propagating across the channel, reflecting from the other side, and interacting destructively with beams propagating from the surface. On the Australian side of the Timor Sea, the generation area was quite broad and beams appeared to fan out from a generation point (3-D image in the auxiliary material). A surface peak occurred midchannel, apparently as a result of constructive interference. In general, extremely strong M_2 and K_1internal tides were generated in Ombai Strait and strong diurnal internal tides were generated on both sides of the Timor Sea.

[43] In conclusion, owing to the intricate topography, the baroclinic response even of the individual tidal constituents was extremely complex with multiple beams being generated and propagating in different directions, interacting either constructively or destructively with themselves and/or other beams. This resulted in highly variable baroclinic tidal fields with large gradients and high-velocity shears both horizontally and vertically.

5.2. Comparison to Available Current Meter Data

[44] Agreement between the model results and the observations varied, with the model estimates generally larger than the corresponding observations. This was expected since the data selection process for the observational data deleted much of the high-velocity data resulting in a low bias for the observations. RMS differences of the tidal ellipses for all the instruments were 4.0, 3.3, 8.0, and 5.8 cm s^{-1} for the M_2, S_2, K_1, and O_1 constituents, respectively. Much of this difference was associated with the uppermost two instruments of MAK-1. When these two instruments were excluded, RMS differences were reduced by ~1 cm s^{-1} with the exception of O_1 (Table 2).

[45] There was excellent agreement for the semidiurnal constituents for MAK-2 (Figure 5c for M_2) with the major

Table 2. RMS Differences for the Four Observational Moorings for the Four Tidal Constituents and the Overall RMS Difference for All Instruments and All Instruments Except the Upper Two on Makassar Mooring MAK-1

	Makassar Mooring MAK-1 (cm s^{-1})	Makassar Mooring MAK-2 (cm s^{-1})	Maluku Mooring (cm s^{-1})	Halmahera Mooring (cm s^{-1})	All Mooring Instruments (cm s^{-1})	All Mooring Instruments Except the Upper Two for MAK-1 (cm s^{-1})
M_2	5.4	3.5	3.2	2.1	4.0	2.8
S_2	2.8	1.7	0.5	6.4	3.3	3.1
K_1	9.4	1.3	4.3	1.5	8.0	7.0
O_1	7.4	7.9	1.5	1.8	5.8	4.8

axes replicating the vertical pattern of the observations, all model estimates within the observational uncertainties, and RMS differences of 3.5 and 1.7 cm s^{-1} for M_2 and S_2, respectively. However, the diurnal constituents were not as well replicated. The model estimates peaked about 200 m below the observational peak and the model estimates were all higher than the observations and only at the upper most instrument were the model estimate within the observational uncertainty (Figure 5d for K_1). RMS differences were larger for the diurnal constituents, 11.3 and 7.9 cm s^{-1} for K_1 and O_1, respectively. Agreement was also reasonable for the semidiurnals at MAK-1 (Figure 5a for M_2), though the model estimate peaks slightly higher in the water column, the general structure of the major axes was repeated. RMS differences were 5.4 and 2.8 cm s^{-1} for M_2 and S_2, respectively. Again the diurnals were a different matter. The model did not replicate the general structure of the major axes, although many of the model estimates fell within the observational uncertainty (Figure 5b for K_1). Observational uncertainties were so large, that no comparisons were done above 200 m or below 700 m. It is curious that there were significant differences between the observations for the two locations and particularly between the model estimates for the two locations. These locations were quite close together, ~16 km or 3 model grid cells apart. Grid cells, which are only separated by 2 cells, are likely to experience nearly the same forcing. This highlights the high spatial variability and localized nature of the baroclinic response. Agreement for the diurnals improved at the Maluku and Halmahera moorings (Figures 5e–5h) with lower RMS differences (Table 2). For this region, however, the paucity and spacing of the observational points were insufficient for a definitive model performance evaluation.

[46] Since only 24 layers were used in the model, the model is likely to smooth over, shift, and/or miss some of the internal wave features. The vertical shift in the peak major axes of 200 m is likely attributable to a combination of vertical resolution, both in the model and the observations, and errors in the mooring depths. Horizontal resolution also plays a role in the accuracy of the model estimates. A previous study showed that a resolution of 5 km is sufficient to estimate where internal tides are being generated, but insufficient to accurately replicate the internal tidal fields [*Robertson*, 2006]. Nevertheless, it is useful to have the estimate of the internal tidal fields and a ballpark evaluation their accuracy. It should be mentioned that the complexities of the observational current meter data due to mooring blowdown, reduced their reliability as ground-truth tidal estimates. As a result, some agreement existed between the model estimates and the current meter observations, but no definitive comparison or model performance evaluation could be made on the basis of velocities.

6. Composite Fields

[47] Although the portioning of the tidal velocities by constituent is occasionally useful, many applications primarily require the total velocity, not individual tidal contributions. To focus on the fluctuating portion of the depth-dependent velocity, baroclinic anomalies were calculated by removing the depth-independent velocity from the depth-dependent velocity. Standard deviations were then determined independently for both the U and V velocity anomalies. These standard deviations were combined, estimating the total fluctuations.

6.1. Baroclinic Anomalies

[48] Combined standard deviations of the baroclinic anomalies were calculated along the transects (Figure 11). Velocity fluctuations exceeded 50 cm s^{-1} in Makassar, Lifamatola, and Ombai straits. The combined standard deviations of the baroclinic anomalies were generally larger than the major axes for either the M_2 or K_1 constituents for all of the transects, although influences of the individual constituents were clearly evident. These large values resulted from constructive interference between the constituents. This was particularly true in the regions with low major axes such as the north side of Dewaking Sill and the Banda Sea northwest of Ombai Strait. In these regions, typical M_2 and K_1 major axes were ~1–2 cm s^{-1} (Figures 9c, 9e, 9h, and 9j); however, the combined major axes ranged from 8 to 12 cm s^{-1}, a factor of ~5–10 higher. In a few transects, such as the bottom on the western side of Lifamatola Strait, destructive interference resulted in combined standard deviations smaller than the M_2 major axes. Like the major axes, the combined standard deviations were highly complex and showed strong vertical and horizontal gradients, indicating strong shears in the water column.

6.2. Comparison to Available Current Meter Data

[49] Basic statistical analysis and spectra were performed on the model depth-dependent velocity times series and on the time series from the two Makassar moorings to evaluate how well the model replicated the total velocity variability. Velocity means for the observations and model results showed similar patterns at both Makassar moorings (circles and squares for the U_3 and V_3 velocities, respectively for the observations and crosses and pluses for the U_3 and V_3 velocities, respectively for the modeling results, in Figures 12a and 12b). But there were large discrepancies, particularly above 200 m and for the V_3 velocities at 800

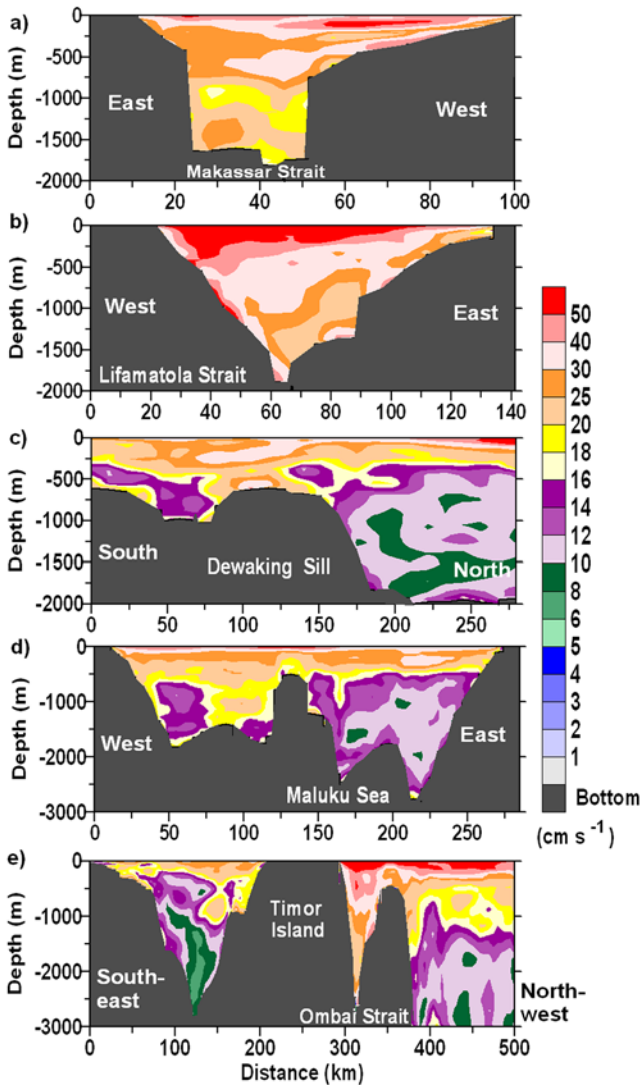

Figure 11. Transects of the combined standard deviations of the V and U baroclinic anomalies in velocity for (a) Makassar Strait, (b) Lifamatola Strait, (c) Maluku Strait, (d) over Dewakang Sill, and (e) Timor and Ombai straits.

and 1000 m on MAK-1. Velocity standard deviations were higher for the model results for both moorings indicating more variability in them by 5–10 cm s^{-1} (circles and squares for the U_3 and V_3, respectively for the observations and crosses and plusses for U_3 and V_3, respectively for the modeling results, in Figures 12c and 12d). Spectral analysis showed velocity fluctuations peaked at the same frequencies, the predominant tidal frequencies, with the same intensity in the model and the observations (Figure 13). The model results had higher spectral energies at low frequencies indicating the higher standard deviations of the model results are likely due to low-frequency fluctuations. The observations showed higher spectral energies at high frequencies on MAK-1 (Figure 13a), particularly at the harmonics of the diurnal and semidiurnal tidal frequencies. These peaks were higher at frequencies that were harmonics of both semidiurnal and diurnal frequencies. The same spectral response occurred for observations at 100 m depth on MAK-2 (Figure 13b), but not deeper in the water column at 675 m (Figure 13c). Since tidal estimates for MAK-1 and the upper 200 m of MAK-2 are less reliable than for the deeper instruments on MAK-2, this high energy at the high frequencies may be a result of the bobbing up and down of the moorings and an indicator of the complexity with the observations or alternatively a surface response. For the more stable mooring, MAK-2, the spectral densities for the model and observations agreed within the 95% confidence levels (dashed lines) for frequencies above 0.025 h^{-1} (Figure 13c). Evidently the model has too much energy at low frequencies and/or the mean. At this resolution, tidal simulations do not replicate mean velocities well [*Robertson*, 2006]; consequently, this low-frequency discrepancy is attributed to the horizontal resolution.

7. Summary

[50] Barotropic and baroclinic tides were simulated for a region of the Indonesian Seas at a ~5 km resolution using ROMS. Four tidal constituents were used for forcing, M_2, S_2, K_1, and O_1 and 15 days of simulated data were generated. Comparisons to various observations confirmed that the simulations replicated the major barotropic and baroclinic tidal responses, although errors did exist. Model results were compared to T/P crossover data to evaluate the barotropic elevation response, T/P along-track data to evaluate the baroclinic elevation response, and current meter measurements on four moorings. Model estimations of elevation amplitudes agreed reasonably well with the T/P crossover observations, with better agreement for the semidiurnal constituents than the diurnal constituents and RMS differences at 12 crossover locations of 7.6 cm for M_2, 5.8 cm for S_2, 11.7 cm for K_1, and 8.8 cm for O_1 for amplitude and 12° for M_2, 21° for S_2, 24° for K_1, and 43° for O_1 for phase. Along-track data indicated M_2 baroclinic tidal activity in several regions, which coincided with a baroclinic response in the M_2 elevation model results. Comparison between the velocity observations and model results were more problematic. In general, the model estimated larger tidal velocities, which is understandable since the current meter observations were biased toward lower values. Again, performance was better for the semidiurnals than the diurnals with RMS differences for all the instruments were 4.0, 3.3, 8.0, and 5.8 cm s^{-1} for the M_2, S_2, K_1, and O_1 constituents, respectively. There was ~1 cm s^{-1} of error associated with the uppermost two instruments of MAK-1 for constituents M_2, S_2, and K_1. On the most stable of the two MAK-2, there was very good agreement for the semidiurnal constituents with the major axes replicating the vertical pattern of the observations, all model estimates falling within the observational uncertainties, and RMS differences of 3.5 and 1.7 cm s^{-1} for M_2 and S_2, respectively. Semidiurnal constituents also agreed well at MAK-1. Model performance for the diurnals was not as good and the model results did not replicate the vertical pattern of the major axis. Some of the difference is attributed to model resolution, both horizontal and vertical. Prior studies have found that the 5 km resolution used is sufficient to identify locations of baroclinic tidal activity, it is insufficient to replicate baroclinic velocities accurately [*Robertson*, 2006]. Accuracy of the bathymetry precluded

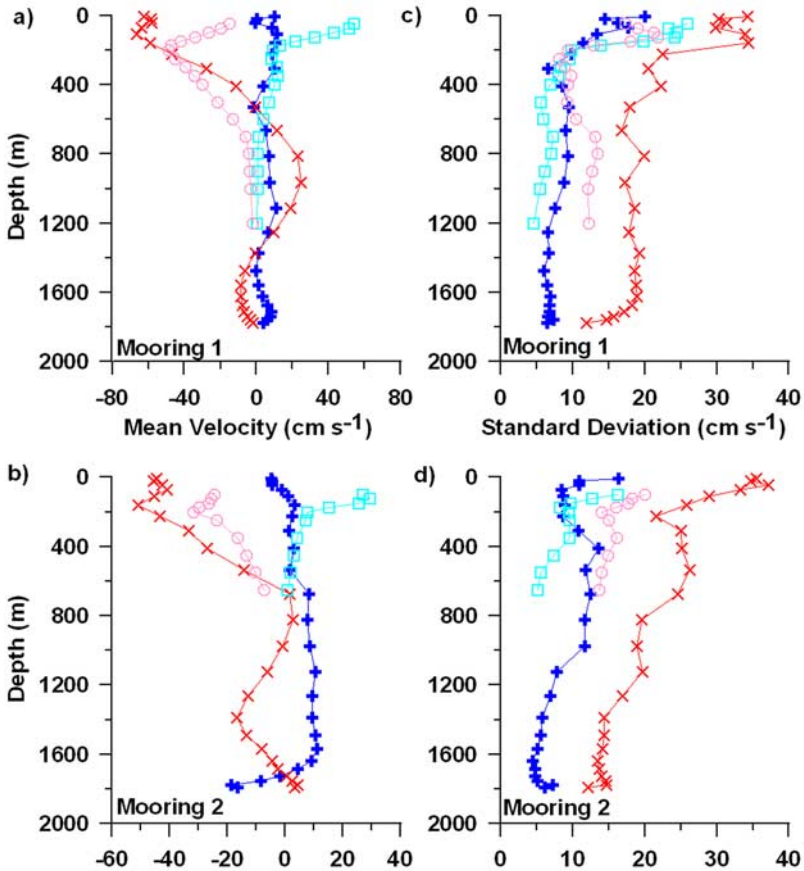

Figure 12. Means of the U and V velocities at Makassar mooring (a) MAK-1 and (b) MAK-2 with observations indicated by squares for the U velocities and circles for the V velocities and model estimates by crosses for the U velocities and pluses for the V velocities. Standard deviations of the V and U velocities at Makassar mooring (c) MAK-1 and (d) MAK-2 with observations indicated by squares for the U velocities and circles for the V velocities and model estimates by crosses for the U velocities and pluses for the V velocities.

higher-resolution simulations. In addition, for the wide range of bathymetry in the Indonesian Seas, the number of vertical levels was inadequate to resolve the location of vertical features, although more vertical structure was apparent in the model results than the observations. However, a more significant source of discrepancy may have been the observations themselves. Logistical difficulties in obtaining observations in this region resulted in high uncertainties in the tidal estimates. Consequently, although qualitatively the agreement between the model results and observations agreed, a definitive comparison and model performance evaluation could not be presently made for the velocities.

[51] The baroclinic tidal response was investigated along five transects. The response was found to be quite complex spatially, in both the horizontal and vertical directions. All four constituents generated internal tides and had strongly depth-dependent major axes, particularly in straits and near rough topography. Beams of internal tides originated from sills and ridges following the path of a typical internal wave ray. Owing to the intricate topography, internal tidal beams seldom propagated without interactions from reflections, beams generated at the same frequency in nearby locations, and/or beams generated by other constituents. Interactions also occurred between the baroclinic and barotropic tides. Both constructive and destructive interference were common in the results. As a result of the rough topography and baroclinic tidal interactions, extremely complex baroclinic tidal fields developed inducing strong shears into the water column.

[52] In the future, it is planned to include wind, solar radiation, dynamic height, and freshwater fluxes corresponding to two cases: the northwest and southeast monsoon seasons. More accurate bathymetric data sets, such as ETOPO-2 [*National Geophysical Data Center*, 2001] will be utilized. Corresponding differences in potential height for these two seasons between the Pacific and Indian oceans will also be included. This will allow more reasonable estimates and quantification of the seasonal effects. As more data become available, for instance from the International Nusantara Stratification (INSTANT) program [*Sprintall et al.*, 2004] in addition to TOPEX/POSEIDON/Jason data, they will be used both for improved initial conditions and for a more definitive model verification and evaluation. Additionally, finer-scale simulations will be performed for specific regions such as Lombok, Ombai, Makassar, and Lifamatola straits,

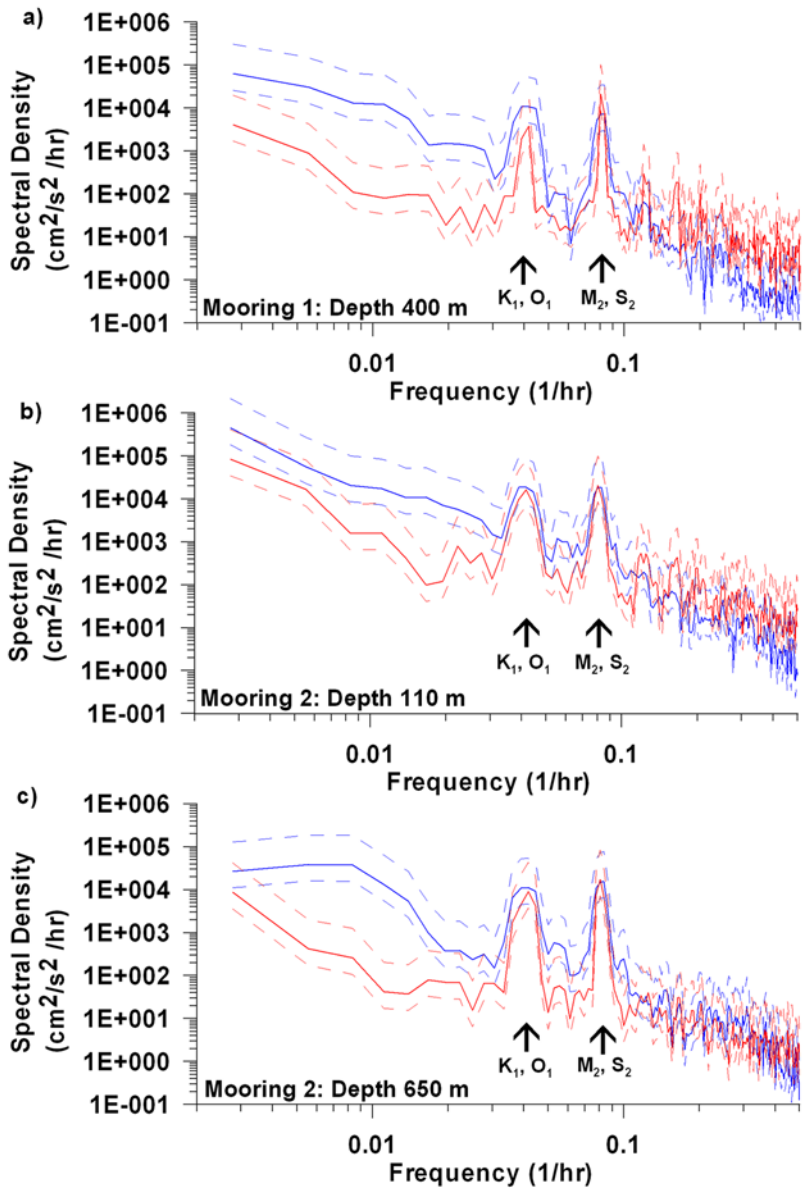

Figure 13. Spectra of the north-south horizontal velocity component at (a) 400 m depth at Makassar mooring MAK-1 location and (b) 111 m depth and (c) 975 m depth at Makassar mooring MAK-2 location with the observational values indicated by black lines and the model estimates by gray lines. The 95% confidence intervals are indicated by the dashed lines in the corresponding color.

Dewaking Sill, and the Timor passage in order to obtain more accurate estimation of the internal wavefields.

[53] **Acknowledgments.** Funding for this work has been provided by ONR through grant N00014-03-1-0423. We also appreciate the efforts and comments of two anonymous reviewers.

References

Anderson, O. B., P. L. Woodworth, and R. A. Flather (1995), Intercomparison of recent ocean tide models, *J. Geophys. Res.*, *100*, 25,261–25,282, doi:10.1029/95JC02642.

Cresswell, G. R., and J. L. Luick (2001), A note on current measurement in the Halmahera Sea, *J. Geophys. Res.*, *106*, 13,945–13,951, doi:10.1029/2000JC000688.

Egbert, G. D., and S. Erofeeva (2002), Efficient inverse modeling of barotropic ocean tides, *J. Atmos. Oceanic Technol.*, *19*, 183–204, doi:10.1175/1520-0426(2002)019<0183:EIMOBO>2.0.CO;2.

Ffield, A., and A. L. Gordon (1992), Vertical mixing in the Indonesian Thermocline, *J. Phys. Oceanogr.*, *22*, 184–195, doi:10.1175/1520-0485(1992)022<0184:VMITIT>2.0.CO;2.

Ffield, A., and A. L. Gordon (1996), Tidal mixing signatures in the Indonesian Seas, *J. Phys. Oceanogr.*, *26*, 1924–1935, doi:10.1175/1520-0485(1996)026<1924:TMSITI>2.0.CO;2.

Ffield, A., and R. Robertson (2006), Indonesian Seas finestructure variability, *Oceanography*, *18*, 108–111.

Ffield, A., and R. Robertson (2008), Temperature finestructure in the Indonesian Seas, *J. Geophys. Res.*, doi:10.1029/2006JC003864, in press.

Flather, R. A., and R. Proctor (1983), Prediction of North Sea storm surge using numerical models: Recent developments in the UK, in *North Sea Dynamics*, edited by J. Sundermann and W. Lenz, pp. 299–317, Springer, New York.

Foreman, M. G. G. (1977), Manual for tidal height analysis and prediction, *Pac. Mar. Sci. Rep. 77-10*, 58 pp., Inst. of Ocean Sci., Sidney, B.C., Canada.

Foreman, M. G. G. (1978), Manual for tidal current analysis and prediction, *Pac. Mar. Sci. Rep. 78-6*, 70 pp., Inst. of Ocean Sci., Sidney, B.C., Canada.

Garrett, C. (2003), Internal tides and ocean mixing, *Science*, *301*, 1858–1859.

Gordon, A. L. (2005), Oceanography of the Indonesian Seas and their throughflow, *Oceanography*, *18*, 14–27.

Gordon, A., et al. (2006), The first 1.5 years of INSTANT data reveal the complexities of the Indonesian Throughflow, *CLIVAR Exchanges*, *11*(4), 10–11.

Hatayama, T. (2004), Transformation of the Indonesian throughflow water by vertical mixing and its relation to tidally generated internal waves, *J. Oceanogr.*, *60*, 569–585, doi:10.1023/B:JOCE.0000038350.32155cb.

Hatayama, T., T. Awaji, and K. Akitomo (1996), Tidal currents in the Indonesian Seas and their effect on transport and mixing, *J. Geophys. Res.*, *101*, 12,353–12,373, doi:10.1029/96JC00036.

Hautala, S., J. Reid, and N. Bray (1996), The distribution and mixing of Pacific water masses in the Indonesian Seas, *J. Geophys. Res.*, *101*, 12,375–12,389, doi:10.1029/96JC00037.

Koch-Larrouy, A., G. Madec, P. Bouruet-Aubertot, T. Gerkema, L. Bessiéres, and R. Molcard (2007), On the transformation of Pacific water into Indonesian Throughflow water by internal tidal mixing, *Geophys. Res. Lett.*, *34*, L04604, doi:10.1029/2006GL028405.

Luick, J. L., and G. R. Cresswell (2001), Current measurements in the Maluku Sea, *J. Geophys. Res.*, *106*, 13,953–13,958, doi:10.1029/2000JC000694.

Martinsen, E. A., and H. Engedahl (1987), Implementation and testing of a lateral boundary scheme as an open boundary condition in a barotropic ocean model, *Coastal Eng.*, *11*, 603–627, doi:10.1016/0378-3839(87)90028-7.

Mazzega, P., and M. Bergé (1994), Ocean tides in the Asian semienclosed seas from TOPEX/POSEIDON, *J. Geophys. Res.*, *99*, 24,867–24,881, doi:10.1029/94JC01756.

Molcard, R., M. Fieux, and F. Syamsudin (2001), The throughflow within Ombai Strait, *Deep Sea Res., Part I*, *48*, 1237–1253, doi:10.1016/S0967-0637(00)00084-4.

Munk, W., and C. Wunsch (1998), The moon and mixing: Abyssal recipes II, *Deep Sea Res., Part I*, *45*, 1977–2010, doi:10.1016/S0967-0637(98)00070-3.

National Geophysical Data Center (2001), ETOPO2 Global 2' Elevations [CD-ROM], Boulder, Colo. (Available at http://www.gfdl.noaa.gov/products/vis/data/datasets/etopo2_topography.html)

Pawlowicz, R., R. Beardsley, and S. Lentz (2002), Classical tidal harmonic analysis with error analysis in MATLAB using T-Tide, *Comput. Geosci.*, *28*, 929–937, doi:10.1016/S0098-3004(02)00013-4.

Ray, R. D., and G. T. Mitchum (1997), Surface manifestation of internal tides in the deep ocean: Observations from altimetry and island gauges, *Prog. Oceanogr.*, *40*, 135–162, doi:10.1016/S0079-6611(97)00025-6.

Ray, R. D., G. D. Egbert, and S. Erofeeva (2005), Brief overview of tides in the Indonesian Seas, *Oceanography*, *18*, 74–79.

Robertson, R. (2005a), Barotropic and baroclinic tides in the Ross Sea, *Antarct. Sci.*, *17*, 107–120, doi:10.1017/S0954102005002506.

Robertson, R. (2005b), Barotropic and baroclinic tides in the Weddell Sea, *Antarct. Sci.*, *17*, 461–474, doi:10.1017/S0954102005002890.

Robertson, R. (2006), Modeling internal tides over Fieberling Guyot: Resolution, parameterization, performance, *Ocean Dyn.*, *56*, 430–444, doi:10.1007/s10236-006-0062-5.

Robertson, R., and A. Ffield (2005), M_2 baroclinic tides in the Indonesian Seas, *Oceanography*, *18*, 62–73.

Robertson, R., A. Beckmann, and H. Hellmer (2003), Tidal dynamics in the Ross Sea, *Antarct. Sci.*, *15*, 41–46, doi:10.1017/S0954102003001044.

Schiller, A. (2004), Effects of explicit tidal forcing in an OGCM on the water-mass structure and circulation in the Indonesian throughflow region, *Ocean Modell.*, *6*, 31–49, doi:10.1016/S1463-5003(02)00057-4.

Shchepetkin, A. F., and J. C. McWilliams (2003), A method for computing horizontal pressure-gradient force in an ocean model with nonaligned vertical coordinates, *J. Geophys. Res.*, *108*(C3), 3090, doi:10.1029/2001JC001047.

Smith, W. H. F., and D. T. Sandwell (1997), Global seafloor topography from satellite altimetry and ship depth soundings, *Science*, *277*, 1956–1962, doi:10.1126/science.277.5334.1956.

Sprintall, J., S. Wijffels, A. L. Gordon, A. Ffield, R. Molcard, R. D. Susanto, I. Soesilo, J. Sopaheluwakan, Y. Surachman, and H. M. van Aken (2004), INSTANT: A new international array to measure the Indonesian Throughflow, *Eos Trans. AGU*, *85*(28), 369–376.

Susanto, R. D., and A. L. Gordon (2005), Velocity and transport of the Makassar Strait throughflow, *J. Geophys. Res.*, *110*, C01005, doi:10.1029/2004JC002425.

Susanto, R. D., A. L. Gordon, J. Sprintall, and B. Herunadi (2000), Intraseasonal variability and tides in Makassar Strait, *Geophys. Res. Lett.*, *27*, 1499–1502, doi:10.1029/2000GL011414.

Umlauf, L., and H. Burchard (2003), A generic length-scale equation for geophysical turbulence, *J. Mar. Res.*, *61*, 235–265, doi:10.1357/002224003322005087.

Umlauf, L., H. Burchard, and K. Hutter (2003), Extending the κ-ω turbulence model toward oceanic applications, *Ocean Modell.*, *5*, 195–218, doi:10.1016/S1463-5003(02)00039-2.

Warner, J. C., C. R. Sherwood, H. G. Arango, B. Butman, and R. P. Signell (2005), Performance of four turbulence closure methods implemented using a generic length scale method, *Ocean Modell.*, *8*, 81–113, doi:10.1016/j.ocemod.2003.12.003.

A. Ffield, Earth and Space Research, 290 Clausland Mountain Road, Upper Grandview, NY 10960, USA.

R. Robertson, Australian Defence Force Academy, University of New South Wales, Northcott Drive, Canberra, ACT 2617, Australia. (r.robertson@adfa.edu.au)